Northward Gulf Stream Migration During the Little Ice Age Revealed Using Monthly-Scale Geochemistry of a Bermudan Stalagmite

EDWARD CHRISTOPHER GRANT FORMAN

NORTHWARD GULF STREAM MIGRATION DURING THE LITTLE ICE AGE REVEALED USING MONTHLY-SCALE GEOCHEMISTRY OF A BERMUDAN STALAGMITE

THESIS

submitted in fulfilment

of the requirements for the degree of

Master of Science

by Research

by

Edward C. G. Forman

Department of Earth Sciences

Durham University

2024

ABSTRACT

Northward Gulf Stream Migration During the Little Ice Age Revealed Using Monthly-scale Geochemistry of a Bermudan Stalagmite

Edward C. G. Forman

The Gulf Stream (GS) forms part of the upper-ocean limb of the Atlantic Meridional Overturning Circulation (AMOC) and plays a vital role in redistributing heat northward, greatly influencing regional climates, and is likely why the Northern Hemisphere is approximately 1.4°C warmer than the Southern Hemisphere. However, anthropogenic warming is weakening the AMOC and as a result it is approaching collapse, which would have profound impacts on regional and global climate. Understanding GS path and strength variability on longer timescales is vital to contextualise its current day weakening and fully appreciate its sensitivity to forcing. This study provides evidence that the GS began migrating northward in the early 1700s. A robust chronology for a Bermuda stalagmite was developed by modelling annual geochemical cyclicity to the mean radiocarbon growth rate and yielded a magnesium concentration record spanning five centuries (1456–2013 CE). Temperature estimates were derived by calibrating the reconstruction to a published coralline sea surface temperature record. The resultant palaeo-oceanographic temperature reconstruction presented here indicates that the GS was likely further south during the Little Ice Age (LIA); however, the compounded effects of weaker westerlies during the pre-1700 extended negative North Atlantic Oscillation (NAO) phase obscure inferences about its exact southward positional extent. This study suggests that a combination of reduced GS transport, enhanced Labrador Current and Deep Western Boundary Current transport, and an extended negative NAO phase, caused the Gulf Stream to be at lower latitudes during the LIA, before migrating northward as the LIA abated. An earlier GS weakening could indicate that the system is more sensitive to additional forcing than previously thought, meaning a tipping event may occur earlier than forecasted. These results may help to guide and constrain predictions made about future Atlantic Ocean circulatory states as well as provide an insight into the climate during the LIA.

TABLE OF CONTENTS

This thesis is dedicated to my late companion and friend, Jack.

TABLE OF FIGURES

LIST OF ABBREVIATIONS

AMOC	Atlantic Meridional Overturning Circulation
CE	Coefficient of Efficiency
COPRA	COnstructing Proxy Records from Age models
DCF	Dead Carbon Fraction
DTW	Dynamic Time Warping
DW	Durbin-Watson test
DWBC	Deep Western Boundary Current
GS	Gulf Stream
LC	Labrador Current
LIA	Little Ice Age
NAO	North Atlantic Oscillation
PCP	Prior Calcite Precipitation
RE	Reduction of Error
SST	Sea Surface Temperature
ST	Signs Test
WRI	Water-Rock Interactions

DECLARATION

This thesis, presented for the degree Master of Science by Research, is my own work, except where acknowledgement is made in text, and is not substantially the same as any work that has been previously submitted to any other university or degree.

However, a version of this thesis has been submitted for publication (myself as lead author). Thus, co-authors external to my supervisory team have provided feedback and input which altered this thesis:

Robert A. Jamieson[1]; Franziska A. Lechleitner[2]; Izabela W. Walczak[3]; Daniel C. Nita[4]; Struan R. Smith[5]; David A. Richards[4]; Lisa M. Baldini[6]; Wolfgang Müller[7]

[1] Earth Surface Science Institute, School of Earth and Environment, University of Leeds, Leeds, LS2 9JT, United Kingdom.

[2] Department of Chemistry, Biochemistry and Pharmaceutical Sciences, and Oeschger Centre for Climate Change Research, University of Bern, Bern, 3012, Switzerland.

[3] Durham Centre for Academic Development, Durham University, Durham, DH1 1TA, United Kingdom.

[4] School of Geographical Sciences, University of Bristol, Bristol, BS8 1SS, United Kingdom.

[5] Natural History Museum, Bermuda Aquarium Museum and Zoo, Bermuda.

[6] School of Health & Life Sciences, Teesside University, Middlesbrough, TS1 3BX, United Kingdom.

[7] Institute of Geosciences, Goethe University Frankfurt, 60438 Frankfurt am Main, Germany.

Edward C. G. Forman
Durham University
2nd September 2024

ACKNOWLEDGMENTS

First and foremost, special thanks go to James Baldini, my supervisor, who, right from the start, offered invaluable guidance and support, and answered countless questions no matter how trivial. Without his expertise and patience, the thesis and manuscript would not have been possible, and I would not have presented at an international conference (EGU24) – something I would never have thought I would do. Thanks are due to my manuscript co-authors, Bob Jamieson, Franzi Lechleitner, Iza Walczak, Dan Nita, Robbie Smith, David Richards, Lisa Baldini, and Wolfgang Müller for their insightful comments, feedback, and guidance. Thanks to Seb Breitenbach, who helped me with the use of the COPRA algorithm; thanks to Paola Moffa-Sánchez, who discussed and improved my ideas for the interpretation of the record; and thanks to my friends and family who have always supported me in my studies and provided a distraction from work when needed.

THESIS CONTEXT

This work aims to build upon two prior theses: Walczak (2016) and Jamieson (2017). The stalagmite used here, BER-SWI-13, was collected in 2013. Milling and sectioning was performed during these previous projects. Walczak (2016) constructed a chronology based on thirteen obtained U-series dates and derived oxygen and carbon stable isotope records. The records were used to reconstruct past climate and tropical cyclone activity, and showed average activity during the industrial period had not surpassed long-term natural variability. Jamieson (2017) similarly used a U-Th chronology, but extracted trace element records, namely Mg, P, Sr, and Ba. Mg and P showed significant correlations with NAO state. Mg likely via changes in effective rainfall influencing their concentrations in the stalagmite through PCP, while P variability is suggested to be related to changes in bioproductivity in the soil or surface vegetation resulting from precipitation changes.

However, since these works, an updated chronology using radiocarbon techniques found that the stalagmite record may be younger than U-Th methods would suggest. Additionally, the cave's connection to the ocean indicates the possibility of using the stalagmite to

reconstruct regional sea surface temperature and Bermuda's position within current day Gulf Stream variability means it has the potential to capture previous ocean current states. This study, therefore, updates the chronology using a magnesium cycle count within radiocarbon age errors and assesses Gulf Stream variability throughout the new record, and hence means the interpretations of the previous theses are beyond the scope of this work.

Due to this study following on from previous work, elements of it are derived from the two foundational theses. Sections 4.1, 4.2, and 4.3 present work from these older studies, while the remainder of this thesis reflects work carried out during this project.

1 INTRODUCTION

The Atlantic Meridional Overturning Circulation (AMOC) is a system of ocean currents which leads to the redistribution of heat latitudinally. Warm near-surface waters travel northward until they reach such high latitudes that they cool, undergo buoyancy loss, and return southward at depth (Buckley and Marshall, 2016). This northward heat transport is in the order of 0.5 petawatts and is thus a key driver of regional climate across the Atlantic (Buckley and Marshall, 2016).

One component of the AMOC is the Gulf Stream (GS), which transports warm water from the Gulf of Mexico northward towards Northwest Europe (Figure 1). Due to its presence, at least in part, winter surface air temperatures in western Europe are up to 10°C higher than the zonal mean at comparable latitudes (Palter, 2015). As an element of the AMOC, the path and strength of the GS is intrinsically linked to the strength of the AMOC as a whole. A weaker AMOC results in a reduced Deep Western Boundary Current (DWBC), a weaker northern recirculation gyre and a northward shift of the GS separation point (Caesar et al., 2018). Anthropogenic warming has caused the AMOC to be at its weakest in the last millennium leading to a northward migration in the Gulf Stream North Wall since at least 1965 CE (Caesar et al., 2021; Seidov et al., 2019). This not only causes a change to the usual distribution of heat, but under enough AMOC weakening can induce regional cooling. Modelling has warned of an AMOC collapse as early as 2057 CE with a rate of cooling post-collapse of 1–2°C per decade in Northern Europe (Ditlevsen and Ditlevsen, 2023; van Westen et al., 2024). Although studies have traced the effects of modern-day positional shifting in temperature records from the Gulf of Maine, whereby a northward GS causes regional sea surface temperature (SST) to rise (Whitney et al., 2022), GS position on longer

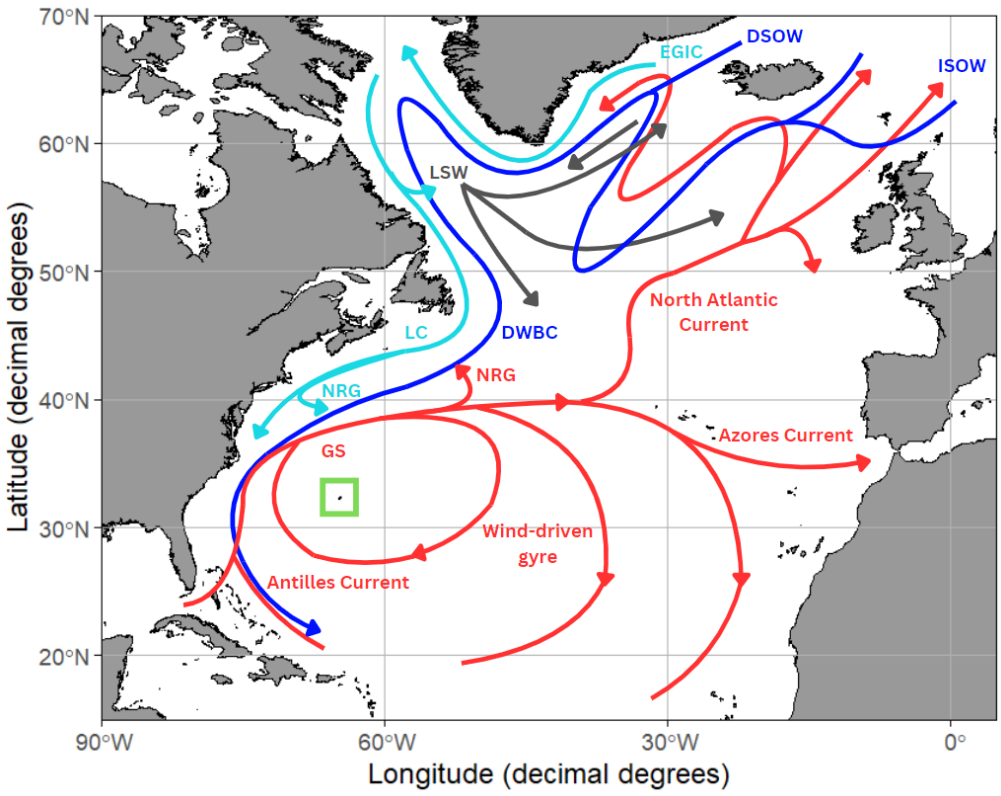

Figure 1: Schematic of North Atlantic AMOC-related ocean currents. The green box highlights the study area, Bermuda. Line colours: red, warm surface currents; blue cold deep currents; cyan, fresh and cold currents; dark grey, spreading of Labrador Sea Water. Abbreviations used: NRG, Northern Recirculation Gyre; LC, Labrador Current; DWBC, Deep Western Boundary Current; IC, Irminger Current; EGIC, East Greenland-Irminger Current; LSW, Labrador Sea Water; ISOW, Iceland-Scotland Overflow Water; DSOW, Denmark Straits Overflow Water. Adapted from Little et al. (2019).

timescales remains poorly constrained. By understanding the effects of previous climatic events on the GS, it is possible to better constrain forecasts of the GS under anthropogenic forcing.

One key time period in the realisation of the GS is the Little Ice Age, a time interval characterised by an extended Northern Hemisphere cold period that occurred between the 1300s and 1800s. It has been argued that increased Arctic sea ice export led to North Atlantic cooling resulting in reduced meridional heat transport by the AMOC (Lapointe and Bradley, 2021). It is thought that the GS was also weaker during the

Little Ice Age (LIA) as well as further south, due to a stronger Labrador Current (LC) and recirculation gyre (Lund et al., 2006; Rashid et al., 2023; Thibodeau et al., 2018). Lund et al. (2006) estimated the volume transport of the Florida Current for the last 1100 years using fourteen cores from the Florida Straits and found the Gulf Stream to have been 10% weaker during the LIA. Due to the LIA occurring outside the range of instrumental records, palaeoclimate reconstructions are crucial to make inferences about GS transport and path.

Proxy-based reconstructions have been obtained from archives including: corals (e.g., Goodkin et al., 2008; Saenger et al., 2009), ice cores (e.g., Osman et al., 2019), sediment cores (e.g., Black et al., 2007), speleothems (e.g., Baldini et al., 2015; Mangini et al., 2005), sclerosponges (e.g., Swart et al., 2002; Waite et al., 2020), and tree rings (e.g., Cook et al., 2013; Salzer and Kipfmueller, 2005). These archives provide a unique insight into palaeoclimatic and palaeoenvironmental changes by recording variables such as: atmospheric composition (e.g., Ahn et al., 2012), ocean acidity (e.g., Wei et al., 2009), precipitation (e.g., Yan et al., 2011), temperature (e.g., Mann et al., 2008), and volcanic activity (e.g., Zielinski, 2000).

Stalagmites are increasingly providing important constraints on palaeoclimate, particularly due to their amenability to accurate and precise age dating and potential for high-resolution records, in some cases at monthly timescales. Strong environmental seasonality can preserve visible or geochemical laminations, offering high-precision chronological information, complementing any radiometric chronological model (Baker et al., 2021; Carlson et al., 2018). Magnesium (Mg) concentrations in stalagmites can yield a seasonal geochemical signal (e.g., Carlson et al., 2018; Huang et al., 2001; Wong et al., 2011). For this reason, stalagmite Mg records can yield a climate proxy through their concentrations, which can also yield chronological information via seasonal cyclicity. Mg concentrations are sensitive to effects of prior calcite precipitation (PCP) and so are often used as a rainfall proxy (e.g., Cisneros et al., 2021; Jia et al., 2022; Wassenburg et al., 2020). However, areas with consistent high rainfall usually do not exhibit a strong PCP effect meaning that Mg concentration variability is likely not indicative of rainfall change (Denniston et

al., 2013; Jia et al., 2022). Stalagmite Mg concentrations can also record temperature based on the temperature dependency of Mg's partition coefficient (D_{Mg}) in calcite (e.g., Carlson et al., 2018; Drysdale et al., 2020). Drawing on the known temperature control on Mg's fractionation, stalagmites in northern Tuscany, southern Brazil, Germany, and Morocco (among others) have yielded Mg-temperature reconstructions (Cruz et al., 2007; Drysdale et al., 2020; Riechelmann et al., 2012). However, sea spray contributions to rainfall may also affect dripwater especially in island karst systems and, consequently, stalagmite Mg concentrations (Baldini et al., 2015; Fairchild et al., 2000; Sinclair et al., 2012; Tremaine et al., 2016).

Bermuda's extensive cave systems and position within the recirculation gyres south of the GS, make it an ideal location for capturing the effects of a southward shift of the GS. Annual palaeotemperature records for Bermuda do exist such as Goodkin et al. (2008) (1781–1999) and Kuhnert et al. (2002) (1520–1603); however, a continuous annual SST record for Bermuda spanning more than three centuries remains unavailable. Understanding the palaeoclimatic changes experienced in Bermuda on this temporal scale will provide a new insight into how the LIA, with its clearly expressed Northern Hemisphere climate anomaly, affected the GS (Broecker, 2000; Lapointe and Bradley, 2021; Lund et al., 2006; Schleussner et al., 2015; Wanner et al., 2022).

This study examines the composition of a stalagmite (BER-SWI-13) from Bermuda to derive a high-resolution palaeotemperature record. Using a geochemical cycle count, aided by radiocarbon chronological constraints, and a Cochrane-Orcutt regression, this thesis presents an SST reconstruction spanning more than five centuries. The study aims to use these data to get a new perspective on North Atlantic Ocean variability during the LIA as well as consider the potential changes in the GS throughout the record.

2 BACKGROUND

2.1 STALAGMITES AS CLIMATE ARCHIVES

Calcareous stalagmites are one example of a climate archive. Known for their ability to provide continuous, precisely dated time series of time spans between 10^3–10^5 years, unaffected by post-depositional diagenetic alterations, they have become a major contributor to palaeoclimatic reconstructions (Fairchild et al., 2006). Stalagmites grow upwards as crystallised deposits of calcium carbonate ($CaCO_3$) in karstic caves and are typically fed by an overhanging stalactite. They form due to the CO_2 degassing of percolating waters from the overlying soil and bedrock surfaces. Because these waters vary seasonally, stalagmites can also preserve intra-annual climate variability. The power of stalagmites as climate archives is twofold: the variety of accurate and precise dating methods as well as the range of available proxies. Together these properties coalesce to yield some remarkable palaeoclimatic reconstructions.

Stalagmite chronologies are principally formed from three methods: (i) U-Th, (ii) radiocarbon (^{14}C), and (iii) layer counts. The very low ^{230}Th content of drip waters means that any subsequent ^{230}Th accumulation is likely purely the product of radioactive decay of ^{238}U and ^{234}U, making U-series dating of stalagmites particularly robust (van Calsteren and Thomas, 2006). However, because of either low uranium or high detrital Th (Th in dripwater that originates from the overlying rocks or soils and not the radioactive decay of uranium) concentrations, stalagmites are not always able to be accurately dated with this method. Such stalagmites are typically young (< 300 years) or those from tropical cave systems (Faraji et al., 2021; Hodge et al., 2011). In these cases, a best-fit growth rate between the stalagmite ^{14}C data and known atmospheric ^{14}C variability can derive a radiocarbon chronology (Lechleitner et al.,

2016). Stalagmites with limited dead carbon fraction (DCF) variability, a roughly constant growth rate, a measurable ^{14}C decay, and at least one anchor are particularly amenable to this dating method (Lechleitner et al., 2016). Additionally, layer counts can also construct a chronology and usually involve the counting growth laminae or geochemical cycles.

Furthermore, the wide variety of available proxies makes stalagmites able to record multiple environmental parameters at once. Proxies usually arise from varying fractionation rates of stable isotopes (e.g., oxygen and carbon) or trace elements (e.g., Mg, Sr, P), however, petrographic methods are also used. Studies have demonstrated uses for each of these techniques as palaeoenvironmental proxies. For example, oxygen isotope ratios (represented as $\delta^{18}O$) can record changes in rainfall and studies have found phosphorous variability to record bioproductivity.

The limitations of stalagmite-based climate reconstructions arise from the chronology, the proxy used, or the scope/understanding of the stalagmite-derived reconstruction. The technique used or the stalagmite's properties can impede the accuracy of the chronology. U-series and radiocarbon dating both have requirements to make sure they yield correct ages. For example, stalagmites with significant DCF variability cannot yield accurate radiocarbon chronologies (Lechleitner et al., 2016). Additionally, stalagmites with hiatuses or non-linear growth rates can produce chronologies with significant errors if they go undetected. The proxies used can also weaken the reconstructions produced if they are not fully understood due to their variability does not always reflect environmental changes. However, most of these limitations are substantially reduced by using either multiple dating techniques or a multi-proxy approach.

2.1.1 Magnesium as a Proxy

Magnesium is a water-soluble trace element which is readily incorporated into calcite through its substitution with calcium. This substitution mechanism has many controls

and varies with environmental parameters such as temperature and precipitation, thus its potential as a climate proxy has been widely investigated.

Quantifying the rate at which substitution of an element between the carbonate and the parent solution is vital in understanding the drivers behind the element's variability through time. This rate is given by the partition coefficient (D_X) and, in the case of magnesium, is defined as:

$$D_{Mg} = \frac{[Mg/Ca]_{CaCO_3}}{[Mg/Ca]_{aq}}$$

Partition coefficient estimates for speleothem studies arise from laboratory or field experiments (Figure 2). Laboratory studies usually either simulate seawater chemistry or the hydrogeochemical conditions of cave settings, called seawater and cave analogue experiments respectively. For example, Burton and Walter (1991) studied the effects of P_{CO_2} and temperature on magnesium incorporation in calcite using a seawater analogue experiment. Equally, Tremaine and Froelich (2013) derived a D_{Mg}

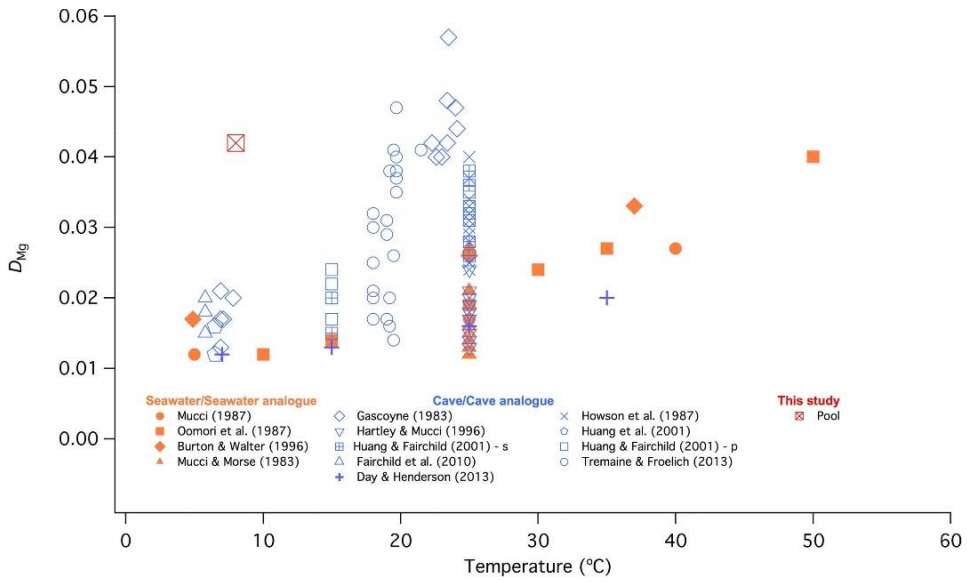

Figure 2: D_{Mg} estimates versus temperature. Taken from Drysdale et al. (2019) and so reference to "This Study" are to Drysdale et al. (2019). Estimates are from a range of published cave and seawater analogue studies.

estimate by studying dripwaters from a cave in Florida and Wassenburg et al. (2020) achieved estimates in a similar way for a variety of caves locations.

The incorporation of Mg depends on five types of factors: (i) atmospheric input; (ii) vegetation/soil; (iii) karstic aquifer; (iv) primary speleothem crystal growth; and (v) secondary alteration (Fairchild and Treble, 2009). Various climate conditions such as temperature, precipitation, and P_{CO_2} can influence the calcite's geochemical signal (Burton and Walter, 1991; Li et al., 2018; Schimpf et al., 2011). Other processes such as prior calcite precipitation (PCP) and water-rock interactions (WRI) can also affect Mg variability. PCP describes the process by which calcite precipitates from solution prior to it reaching the stalagmite leading to increased Mg incorporation due to its low partition coefficient (Treble et al., 2015) and therefore preferential removal of Ca over Mg. PCP occurs as the fluid feeding the stalagmite equilibrates with lower P_{CO_2} conditions along its flowpath (Fairchild et al., 2000). WRI controls Mg partitioning in many ways including incongruent dolomite dissolution and selective leaching, both of which can change the relative abundances of Mg with respect to Ca in the cave environment (Belli et al., 2017; Fairchild et al., 2000). Whereas there are many controls on Mg concentration, there are methods to determine the relative influence of controls external to climatic variations (e.g., PCP vectors; see Section 4.4).

Principally there are three ways Mg is used as a proxy in stalagmites: (i) Mg (ppm), (ii) Mg/Ca, and (iii) δ^{26}Mg. Mg (ppm) describes the concentration of Mg in the calcite. It can be divided by isotope, but this study uses an average of the concentration of ^{24}Mg and ^{25}Mg. Similarly, the Mg concentration can be divided by the Ca concentration to form a ratio within the calcite. Time series in Mg/Ca are often used in subaqueous calcite to show temperature change (Drysdale et al., 2019), but recent studies find it to be a powerful terrestrial temperature proxy too (Duan et al., 2024). Finally, magnesium isotope ratios (i.e., δ^{25}Mg and δ^{26}Mg) can generate insights into variations in stalagmite precipitation rate in response to climate and changing rates of silicate/carbonate weathering (Buhl et al., 2007; Galy et al., 2002; Immenhauser et al., 2010).

Because many of the drivers of Mg concentration variability are controlled by climate, an exact temperature or precipitation estimate may be challenging but relative changes are broadly consistent. For example, drier conditions may have compounded elevations in Mg concentration due to the reduced rainfall having an increased residence time allowing for more WRI (Fairchild et al., 2000). As a result, one of the major limitations is insufficient understanding of what the Mg concentration reconstruction is recording. PCP is one process that can affect a Mg record. However, there are several methods (e.g., PCP vectors in Sr-Mg space) that can account for this by calculating the relative influence of PCP on the stalagmite (Baldini et al., 2015; Oster et al., 2020; Sinclair et al., 2012). Drysdale et al. (2020) also highlighted the power of subaqueous speleothems in this regard as they are not affected by reduced recharge, and thus PCP and/or WRI in the same way. Without these processes impeding the accuracy of their record by exaggerating the climate signal, Drysdale et al. (2020) were able to accurately reconstruct 350,000 years of regional SSTs using the Mg variability of a subaqueous speleothem from a cave in northern Italy.

2.1.2 Other Proxies from Stalagmites

There are many other proxies available for stalagmite-derived climate reconstructions including stable isotopes in addition to other trace elements. Among these are oxygen ($\delta^{18}O$) and carbon ($\delta^{13}C$) stable isotope ratios. Because oxygen isotope fractionation occurs during the phase change and diffusive exchange of isotopes between rain and vapour, it's variability can reflect changes in temperature and rainfall amount (e.g., Baker and Bradley, 2010). Carbon isotope ratios usually reflect changes in the environment around or above the stalagmite and thus can record many different processes (such as atmospheric CO_2 concentrations, vegetation type, amount or productivity, as well as soil and host rock composition) (Genty et al., 2006). Furthermore, there are a variety of other trace elements that can vary in concentration as a result of environmental factors, including strontium, barium, phosphorous, and sulphur. Strontium and barium, in addition to magnesium, are often reported as ratios to calcium and then used to infer rainfall or temperature variability (Fairchild and

Baker, 2012). Studies have found phosphorous records can reconstruct bioproductivity and vegetation amount (Treble et al., 2003); and sulphur concentrations can record variations in anthropogenic and volcanic sulphur supply (Wynn et al., 2008). However, because these proxies are not used in this thesis, they are not discussed in any further detail.

2.2 North Atlantic Climate

North Atlantic climate is driven by many atmospheric and oceanic processes including the strength and direction of the ocean currents and winds, as well as oscillations such as the Atlantic Multidecadal Oscillation (AMO), the Arctic Oscillation (AO), the North Atlantic Oscillation (NAO), and the El Niño-Southern Oscillation (ENSO). Due to the strong proclivity for the Atlantic to redistribute heat from Southern Hemisphere and tropics to the Northern Hemisphere, it plays a vital role in regulating the mean climate state and making regional Northern climates milder and more hospitable (Palter, 2015).

2.2.1 The Atlantic Meridional Overturning Circulation (AMOC)

The AMOC is a system of ocean currents that transports heat from the southern high latitudes over the equator and towards the northern high latitudes. Its northward heat transport even at high southern latitudes makes it unique as an ocean system. For this reason, it is the primary driver behind why the Northern Hemisphere is an average of 1.4°C warmer than the Southern Hemisphere and is thus an important stabiliser of northern climates (Feulner et al., 2013; Little et al., 2019).

However, with temperature and salinity both strongly influencing the direction and strength of these currents it is a highly sensitive system. Due to this it is considered one of the Earth's major climate tipping points. Stommel (1961) first recognised the

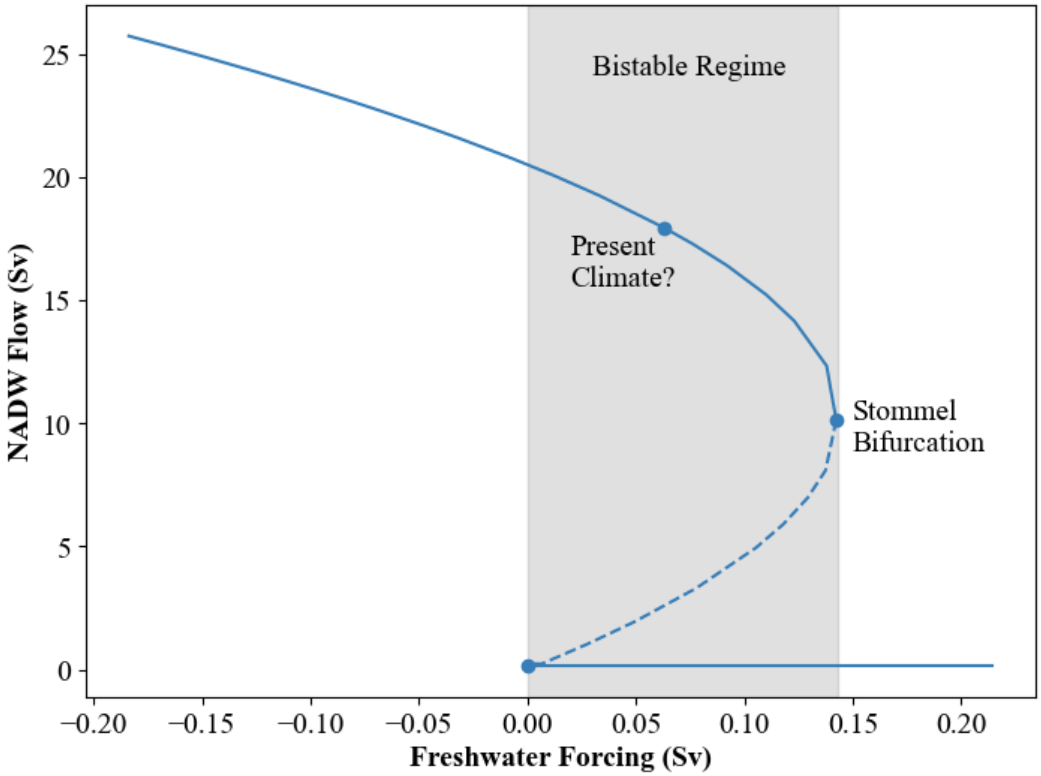

Figure 3: Stommel's box model showing AMOC stability. The solid blue lines show stable equilibrium AMOC states and the dashed line unstable states. Adapted from Rahmstorf (2024) after Stommel (1961).

AMOC's instability to changes in salinity (e.g., a freshwater flux or increased net evaporation) and constructed a box model for the system (Figure 3). It shows that in some states the AMOC exists in a bistable regime whereby dramatic changes in flow strength can occur if freshwater forcing surpasses a threshold (represented by the Stommel Bifurcation in Figure 3). However, if the AMOC is in a monostable regime then this forcing will simply lead to a temporary adjustment before recovering. Although many climate models suggest present climate is within a monostable regime, other analysis (such as those done from climate reconstructions) indicate that the AMOC under modern warming is fast approaching a tipping point (Hofmann and Rahmstorf, 2009).

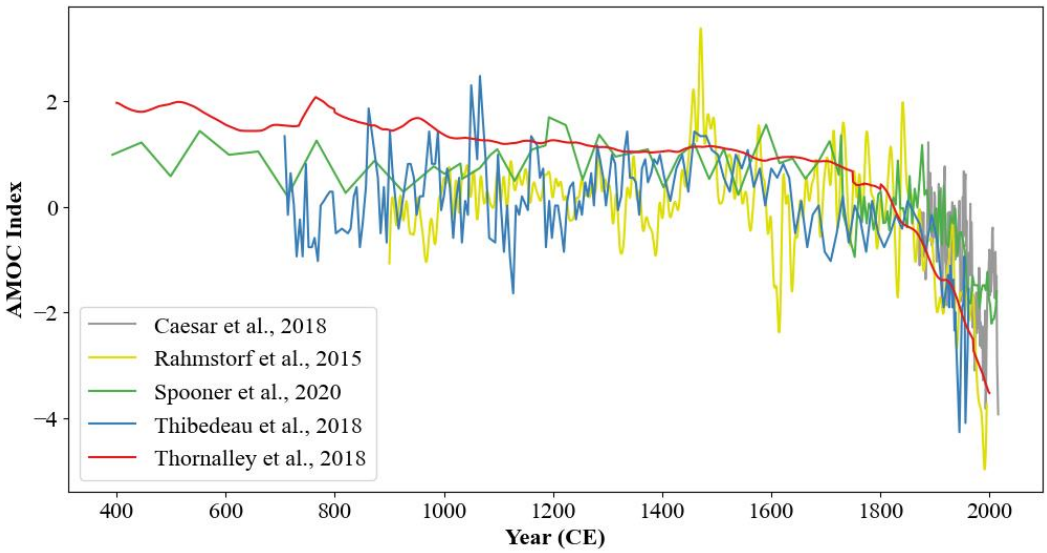

Figure 4: AMOC strength reconstructed using various techniques. AMOC indices were z-scored and adjusted so they plot on the same scale.

Climate reconstructions provide evidence for previous changes in AMOC strength. These primarily take the form of either Dansgaard-Oeschger (DO) or Heinrich events (Rahmstorf, 2002). DO events exhibit spikes of Northern Hemisphere warming on the order of 10–15°C within a decadal timescale (Dansgaard et al., 1982). These events have been attributed to sudden increases in the strength of ocean convection leading to heat circulation further north and warming (Gottschalk et al., 2015). Conversely, Heinrich events are linked to AMOC weakening or shutdown due to their correlation with large degrees of ice mass loss (Marcott et al., 2011).

Due to the severity of the impact of the AMOC shifting between modes, many studies have reconstructed AMOC strength over the past few hundred years to assess the systems likelihood and timing of future collapse. These AMOC proxies usually arise from backcasting climate models or analysing proxy records. Of the many available AMOC indices (Figure 4), three particularly prominent examples are Rahmstorf et al. (2015), Caesar et al. (2018), and Thornalley et al. (2018). Rahmstorf et al. (2015) developed an AMOC index spanning over a millennium from the difference in temperature anomalies between the Northern Hemisphere and the subpolar gyre. They used multi-proxy reconstructions with instrumental data and found evidence of

significant weakening in the 1900s. Caesar et al. (2018) obtained an AMOC index for the post-industrial era using the same definition but using climate model and SST observations, equally finding substantial weakening in the mid-1900s. Thornalley et al. (2018) used the Oceans2k proxy synthesis dataset to construct a T_{sub} AMOC index extending back to ca. 400 AD. From this and other indicators they found evidence of AMOC weakening in the mid-1800s. Changepoint analysis of these, and other, AMOC records found current weakening to be in two phases (Caesar et al., 2021). The first began in the mid-1800s likely in response to enhanced freshwater fluxes at the end of the LIA from the Arctic and Nordic seas (Thornalley et al., 2018). The second decline started in the mid-1900s and is more severe than the first. It likely reflects the influence of anthropogenic warming on the AMOC and Caesar et al. (2018) estimate it to correspond to a weakening of around 15%.

Modelling of future AMOC collapse using reanalysis data in climate models places an AMOC tipping event (τ_e) at dates earlier than previously suggested. The IPCC concluded in their sixth assessment report (AR6) published in 2021 that an AMOC collapse before 2100 CE was unlikely. However, with the melting of the Greenland Ice Sheet occurring at faster rates than anticipated, more recent studies find the tipping event to be closer than 2100 (e.g., Ditlevsen and Ditlevsen, 2023). Ditlevsen and Ditlevsen (2023) performed Maximum Likelihood Estimation (MLE) analysis of the time of tipping on a AMOC fingerprint developed using the aforementioned subpolar gyre definition and reanalysis data to find a best estimate for collapse of 2057 CE with a 95% confidence interval of 2025-2095. Similarly, Smolders et al. (2024) found a 59 ± 17% chance of an AMOC collapse before 2050 CE using probabilistic techniques (mean of 2050 CE; 2037–2064 10–90% confidence interval). Further modelling has shown an AMOC collapse induces a surface temperature cooling trend of between 10–20°C per 100 years in Northern Europe and the Nordic Seas (van Westen et al., 2024). Therefore, constraining the likelihood of collapse, point of collapse, resultant degree of cooling, and further impacts remains a vital area of research.

2.2.2 The North Atlantic Oscillation (NAO)

The North Atlantic Oscillation (NAO) is a principal mode of variability in the North Atlantic region as it reflects changes in surface pressure, thus effecting the direction and strength of Atlantic winds. The NAO index is derived from variations in pressure intensity between the Icelandic Low and the Azores High, the main permanent North Atlantic pressure centres (Raible et al., 2021). This pressure difference controls the strength and direction of the westerlies across Europe, impacting both regional precipitation and temperature. When this difference is large it signifies a positive NAO phase and is characterised by stronger westerlies leading to wetter conditions over Western and Central Europe and dryer conditions over Southern Europe. If the pressure difference is reduced a negative NAO phase ensues causing weaker westerlies and hence dryer conditions over Western and Central Europe and wetter conditions over Southern Europe. However, its effects are also prevalent in North America with a positive NAO phase leading to dryer conditions in Northern Canada and wetter conditions on the East coast of the United States of America. This effect reversed for a negative NAO phase.

NAO variability is a driver of changes in regional surface temperatures, precipitation, sea ice distributions, and ecology (Hurrell et al., 2003). Studies have also shown it can affect the intensity and number of storms with a negative phase being associated with fewer but intensified tropical cyclones (Pinto and Raible, 2012; Trouet et al., 2012). Furthermore, other studies have found a link between the NAO phase and changes in the Nordic Seas circulation patterns (Chaudhuri et al., 2011; Zhang et al., 2020). A positive NAO phase is associated with stronger westerlies and thus enhanced surface heat loss and stronger deep-water formation causing a stronger AMOC (Medhaug et al., 2012). A stronger AMOC can lead to a more northerly GS path. Taylor and Stepens (1998) showed a NAO-GS path connection exists for the recent changes in NAO phase (1993-2016) and that the NAO phase leads GS path displacement by approximately 2 years.

The NOAA has an instrumental NAO index at monthly resolution extending back to 1950. Reconstructions from proxy methods are required to assess NAO state on longer timescales. Of the many available NAO reconstructions, the following have garnered particular attention: (i) Proctor et al. (2000) which reconstructed the NAO using a stalagmite from northwest Scotland; (ii) Luterbacher et al. (2001) which represents the Principal Component Analysis of various documentary and instrumental data; (iii) Trouet et al. (2009) which uses the Proctor et al. (2000) in addition to other proxy records and observational data; and (iv) Ortega et al. (2015) which uses proxy records from an ensemble of multivariate regressions.

2.2.3 Other Controls

Many other phenomena influence climate variability in the North Atlantic including, the Atlantic Multidecadal Oscillation (AMO), the Arctic Oscillation (AO), the El Niño-Southern Oscillation (ENSO), and the Intertropical Convergence Zone (ITCZ). The AMO describes a cycle of average anomalous SSTs in the North Atlantic which has a period of 60–80 years. The AO has decadal to centennial variability affecting wind patterns and is closely related to the NAO, ocean circulation, and ice drift. The ENSO has two phases (warm, El Niño and cold, La Niña) with periodicities of 2–7 years which relate to tropical Pacific SST anomalies and influence other regions via teleconnections. The ITCZ refers to an area of low pressure where the trade winds converge causing increased convection, cloudiness, and precipitation. Because these processes are not discussed further here, they are beyond the scope of this section.

2.3 Project Aims

North Atlantic Ocean states prior to the temporal range of instrumental records remain elusive, and without this knowledge our understanding of future AMOC weakening is hindered. The location of Bermuda and extensive array of climate archives provides a unique opportunity to reconstruct and examine palaeo-oceanographic variability.

This study investigates proxy evidence recorded within a Bermudan stalagmite in the context of regional oceanographic changes and North Atlantic variability. The main objectives of this project are:

- Refine the age model by exploring radiocarbon and cycle count alternatives to U-Th, and in so doing improve the chronology's resolution;
- Revise the Mg record in line with the updated age model;
- Derive a palaeoclimatic temperature reconstruction utilising magnesium's temperature dependency;
- Interpret the geochemical record in terms of North Atlantic climate variability to infer previous ocean states, specifically in terms of AMOC and GS variability.

3 SITE DESCRIPTION

Leamington Cave in north-eastern Bermuda (32° 20’ 31.64” N, 64° 42’ 30.93” W; entrance at 18 m a.s.l.) is a privately-owned former show cave connected to the ocean via flooded conduits connecting to a large cave pool and contains many actively growing speleothems. The Bermudan Islands consist of a carbonate platform above a volcanic seamount and are comprised almost entirely of aeolianites, massive limestones, and palaeosols (Vacher et al., 1995). The Walsingham Formation, an

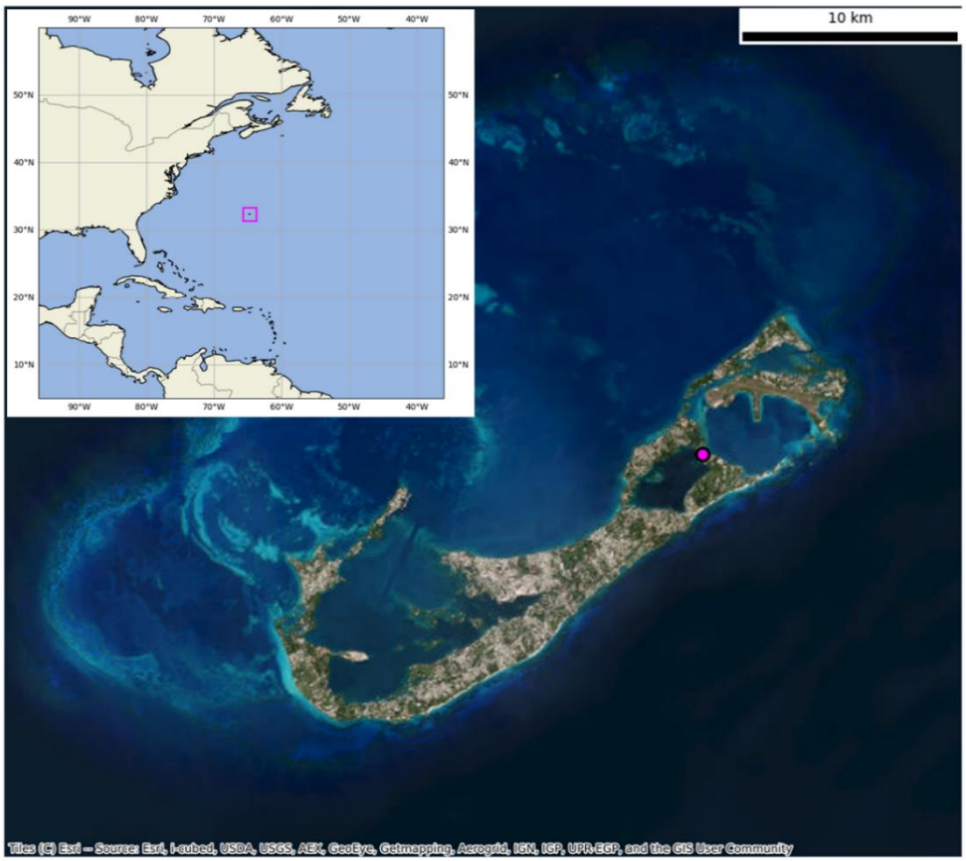

Figure 5: Map of the study site. Aerial view of Bermuda with the location of Leamington Cave marked with a magenta circle. Inset shows Bermuda’s location (magenta box) in the context of the North Atlantic.

aeolianite limestone unit (the oldest limestone unit, deposited approximately 1.1–0.8 Ma), contains most of Bermuda's caves (including Leamington Cave) and outcrops along the eastern border of the Harrington Sound (Hearty and Vacher, 1994; Iliffe and Calderón-Gutiérrez, 2021).

Bermuda has a humid subtropical climate (Cfa in Köppen-Geiger classification (Peel et al., 2007)) and lies within the North Atlantic hurricane belt, with the hurricane season running from June to November each year. Meteorological data (Bermuda Weather Service, 2018) indicate that mean sea temperatures are lowest in February (17.8°C) and peak in August (28.5°C) (Figure 6). May historically experiences the lowest mean monthly rainfall (86.7 mm), whereas October has the highest (161.6 mm) (Bermuda Weather Service, 2018). The hurricane season accounts for a mean of 55% of annual rainfall. Except for September and October, when winds prevail from the east, winds typically come from SW and SSW, reaching a maximum in January (6.01 m/s) and a minimum in September (4.49 m/s) (Bermuda Weather Service, 2018).

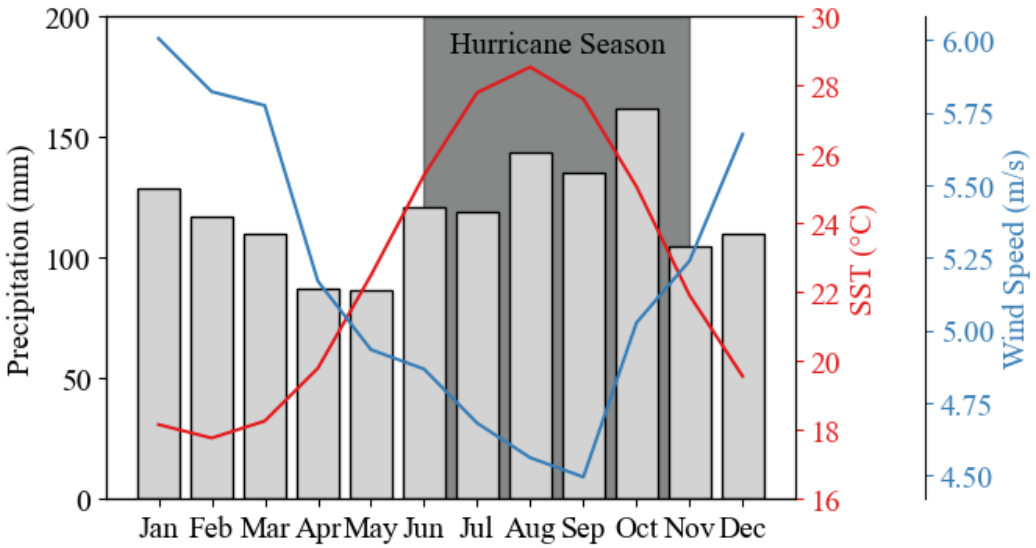

Figure 6: Climate of Bermuda. Sea surface temperature (red; 1950–2018), precipitation (light grey bars; 1949–2018) and wind speed (blue; 1975–1995) averaged monthly (Bermuda Weather Service, 2018). Dark grey area indicates the hurricane season.

4 METHODS

4.1 STALAGMITE BER-SWI-13

BER-SWI-13 is a 192 mm long stalagmite that grew in Leamington Cave, Bermuda. The stalagmite was selected for its favourable internal structure and active drip hydrology, which shows a moderate response to rain events (Walczak, 2016) and plots as a near-ideal seasonal flow (Baldini et al., 2021). Because cave monitoring data revealed a same-day drip rate response to rainfall events (Walczak, 2016), the residence time of the seawater signal is sufficiently low to accurately preserve hydrology-induced seasonality at a monthly-resolution (Baldini et al., 2021). Visual examination showed no signs of growth hiatuses (Figure 7). The cave pool's connection to the ocean promotes daily cave ventilation by tidal flushing, suggesting the stalagmite never experienced condensation corrosion due to CO_2 (Walczak, 2016). Additionally, monitoring data shows daily cave temperature is positively correlated to daily mean SST ($r = 0.83$, $p < 0.01$) (Walczak, 2016).

4.2 U SERIES AND RADIOCARBON DATING

Reconnaissance CT scanning determined the position of stalagmite BER-SWI-13's central growth axis and informed its sectioning. Cut sections were polished and then cleaned in an ultrasonic bath of deionised water (see Walczak (2016) for full methods). Visual examination after sectioning showed no signs of growth hiatuses (Figure 7). Sixteen ~400 mg carbonate powder samples (Appendix 1) were milled along the stalagmite growth axis. These were dated using multi-collector inductively coupled plasma mass spectrometric (MC-ICPMS) U-Th methods at the facilities of Bristol Isotope Group (BIG), University of Bristol, and University of St. Andrews Isotope

Geochemistry (STAiG). U and Th separation and measurement protocols described in Hoffmann et al. (2007) were followed, where CRM U112a and an inhouse Th standard (Teddii) was used for bracketing the samples and correcting for instrumental drift in mass bias, SEM yield. We adopt relevant decay constants from Cheng et al. (2013). U-series data was analysed using the IsoplotR software (Vermeesch, 2018).

U-Th ages for material that is both young (i.e., < 1 ka) and has low $^{238}U/^{232}Th$ ratios are poorly constrained because there is no prior knowledge of the $^{230}Th/^{232}Th$ ratios at the time of calcite precipitation. Because of this, we attempted to assess the initial Th ratio using isochron methods for two of the milled samples (BER-SWI-UTh-13 and -15) by performing replicate analysis (~100 mg sub-samples). However, there was insufficient $^{238}U/^{232}Th$ ratio variation in the two sets of replicate analysis to determine useful estimates of the initial $^{230}Th/^{232}Th$ component.

Most researchers use an estimate of initial Th assuming it is equivalent to bulk Earth silicate composition ($^{238}U/^{232}Th = 0.8 \pm 0.4$). However, there are many examples of elevated values of this ratio where either carbonate dust with high U/Th or hydrogenous elements in cave drip waters have probably influenced the isotopic composition: see review by Richards and Dorale (2003) and recent papers by Wortham et al. (2022) and Huang et al. (2024). Other speleothem samples from the North Atlantic and Caribbean region, including the Bahamas, Yucatan, and Puerto Rico, have been similarly affected (Beck et al., 2001; Fensterer et al., 2012; Hoffmann et al., 2010; Moseley et al., 2015; Rivera-Collazo et al., 2015; Warken et al., 2020).

In the absence of sufficiently robust estimates of the initial Th ratio via isochron methods, we considered the principle of stratigraphic constraint (see Hellstrom, 2006) and adopted an elevated value ($(^{238}U/^{232}Th)_{initial} = 5 \pm 2.5$) that eliminates the major age inversion at the top of the sample (Fig. S3) that is evident when using the bulk Earth initial Th ratios. Using this elevated value also shifts the basal age (BER-SWI-UTh-16) younger and would suggest a growth rate for the oldest material that is closer to that exhibited for the rest of the speleothem. One anomalous age remains for the

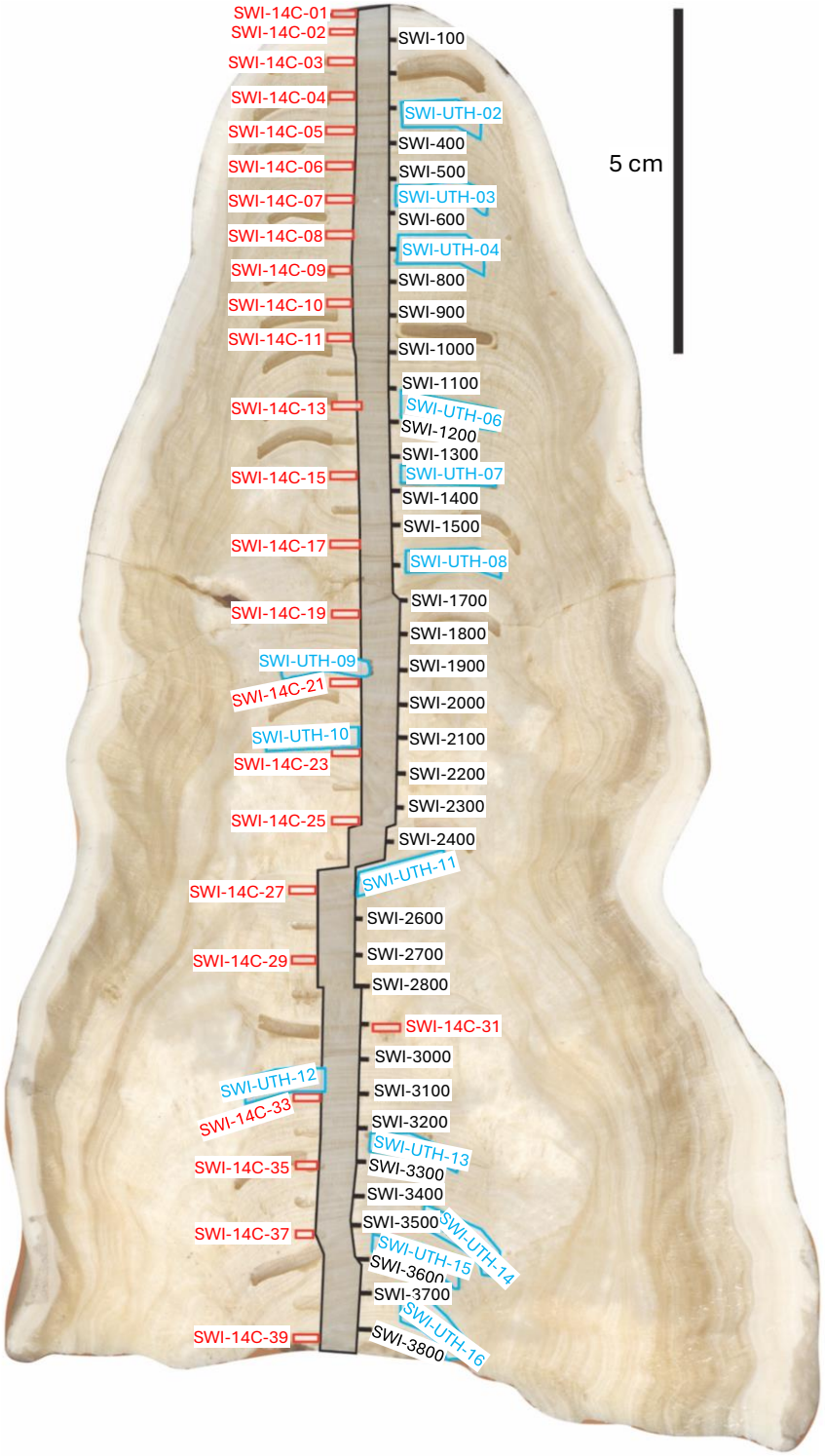

Figure 7: Scan of stalagmite BER-SWI-13. Milling track and dating powder sample positions annotated (U-Th, blue; ^{14}C, red; stable isotopes (not used), black). Trace element transects were performed on the other half (not shown). Figure from Walczak (2016).

sample (BER-SWI-UTh-5), which is likely to have been affected by post-depositional alteration.

Additionally, twenty-five 8–9 mg carbonate powder samples were milled for ^{14}C analysis (Appendix 2) using a semi-automatic high-precision drill (Sherline 5400 Deluxe) at ETH Zurich. The ^{14}C samples were milled in increments of 5 mm for the top 50 mm, and 10 mm for the remaining 140 mm (Walczak, 2016). The top ~0.1 mm was discarded for each ^{14}C sample. Potential contamination during sub-sampling was minimised by cleaning all tools with methanol and drying with compressed air in between samples. Carbonate samples were prepared for accelerator mass spectrometry (AMS) analysis by graphitisation at the Laboratory for Ion Beam Physics (LIP) of ETH Zurich. The samples were processed on an automatic graphitisation system coupled to a carbonate handling system (CHS-AGE, Ionplus, Switzerland) by acidification to CO_2 using 2 mL of 85% H_3PO_4 and followed by graphitisation using excess H_2 over Fe catalyst. Radiocarbon contents were measured on a MICADAS accelerator mass spectrometer (Ionplus) following standard protocols for quality and blank assessment: oxalic acid II (NIST SRM 4990C) was used as the normalising standard, measured to a precision of better than 2‰. We used IAEA-C1 as a blank and IAEA-C2 and a modern coral standard as secondary standards. The procedural blank was established using a ^{14}C-free stalagmite (MAW-1, ~170 kyr old).

4.3 Trace Element Analysis

Trace element concentrations were measured using a prototype RESOlution M-50 excimer (193 nm) laser-ablation system with a two-volume laser-ablation cell coupled to an Agilent 7500ce/cs quadrupole ICPMS at Royal Holloway University, London (Evans et al., 2015; Jamieson, 2017; Müller et al., 2009).

Ablation tracks were pre-ablated to remove any superficial contamination and measured using a 140 by 10 μm rectangular laser slit across 50 mm sectioned blocks on the opposite half to the carbonate sampling. Sectioning was slightly off

perpendicular to the growth direction so that overlaps in transects could compensate for any missing data between sections. A 15 Hz repetition rate and a laser fluence of ~4 J/cm^2 with a stage scan speed of 10 µm s^{-1} of the LA cell were used during the continuous main track measurement (Jamieson, 2017). Speleothem analyses were bracketed by analyses of NIST 612, NIST 610 for quantification using ^{43}Ca as internal standard (Longerich et al., 1996), and MACS3 standards for quality control (see Stoll et al., 2012). The resultant data were then reduced using the lolite software package, using NIST 610/612 standards for external standardisation (Paton et al., 2011).

4.4 BER-SWI-13 CHRONOLOGY

The U-Th chronology suggests an unusually variable speleothem growth rate for a tropical cave environment (124 to 1916 µm yr^{-1}; where the 90th percentile of annual layers in a global review (Baker et al., 2021) is 404 µm yr^{-1}). This variability is most pronounced between depths from top of 106 and 174 mm where the growth rate implied from U-Th dating changes from 1916 to 271 µm yr^{-1} in 68 years. For this reason, this study uses the U-Th chronology only as confirmation when developing an alternative chronology based on radiocarbon dating and annual Mg cycle counting. First, we develop an 'average' chronological model using the radiocarbon-based technique presented in Lechleitner et al. (2016) and refined in Fohlmeister and Lechleitner (2019). This modelling approach uses the radiocarbon data to construct a best fit linear growth rate model, taking into account atmospheric variability in ^{14}C and variability in dead carbon fraction. The chronology produced this way is anchored to a point of known age, which in this case this is given by the clear increase in ^{14}C indicating the rise of the atmospheric bomb spike at 1955 CE (at a depth of 10.179 mm) (Figure 8b). The collection year (2013 CE) provides a second chronological anchor. However, Mg variability is severely dampened after ~1970 CE (Figure 9; standard deviation before 1970: 762 ppm, after 1970: 334 ppm) likely owing to possible localised anthropogenic influences on the stalagmite's drip hydrology (potentially due to the opening of the cave to tourism). As a result, the stalagmite's

growth rate is reduced to an unknown degree, rendering the chronology unreliable. Therefore, the data post-1970 is not used in the interpretations.

The LA-ICPMS-derived magnesium data exhibit well-developed cyclicity through much of the record. A comparison between the Mg cycles and the U-Th and radiocarbon chronologies strongly suggests that the Mg cycles are annual. Multiple Mg cycle counts were conducted to test reproducibility of the counts, and a chronology

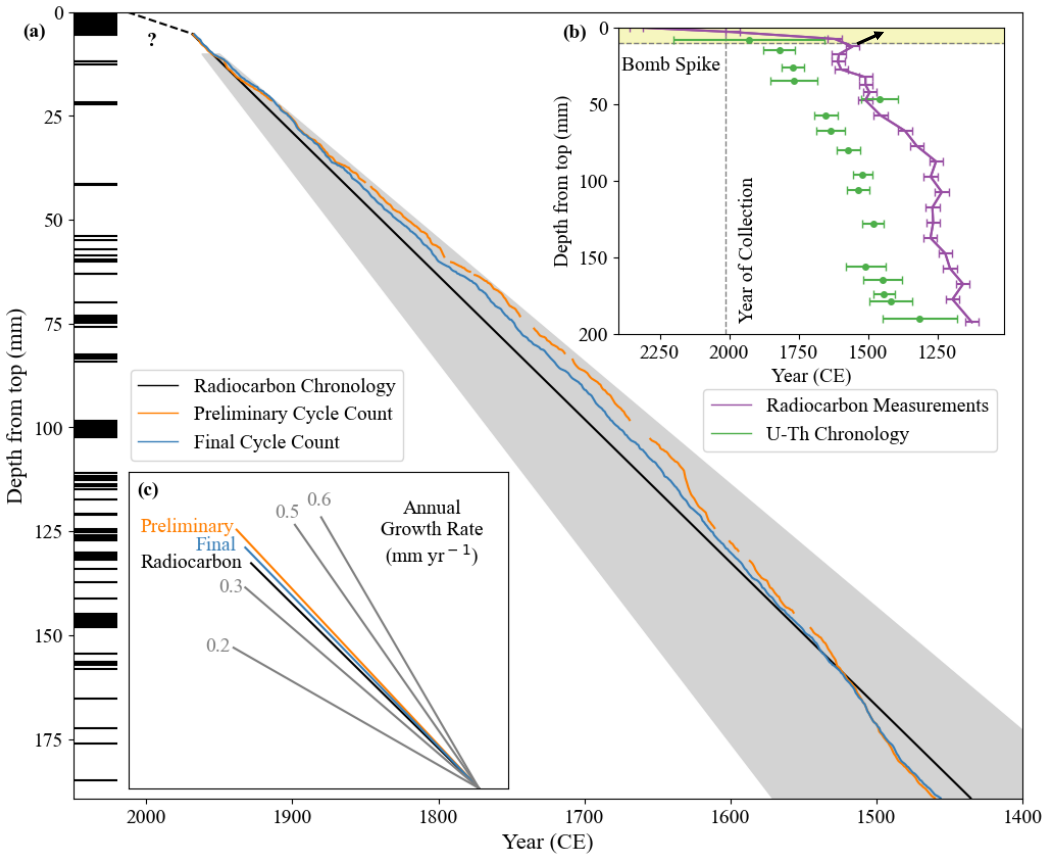

Figure 8: BER-SWI-13 Chronology. (a) Development of the BER-SWI-13 chronology, comparing the preliminary cycle count (orange) and the radiocarbon (black) to the final cycle count (blue) developed from both. Grey shaded area signifies the 2σ confidence interval of the radiocarbon chronology. Black areas (left-hand side) mark depths modelled to the radiocarbon mean. (b) Radiocarbon data recorded in the stalagmite (purple), compared to the U-Th dates (green). Black arrow indicates the trajectory of the radiocarbon data if only influenced by the Suess Effect. (c) Mean growth rates based on radiocarbon (black, 0.345 mm yr^{-1}), preliminary (orange, 0.373 mm yr^{-1}), and final (blue, 0.360 mm yr^{-1}) chronologies.

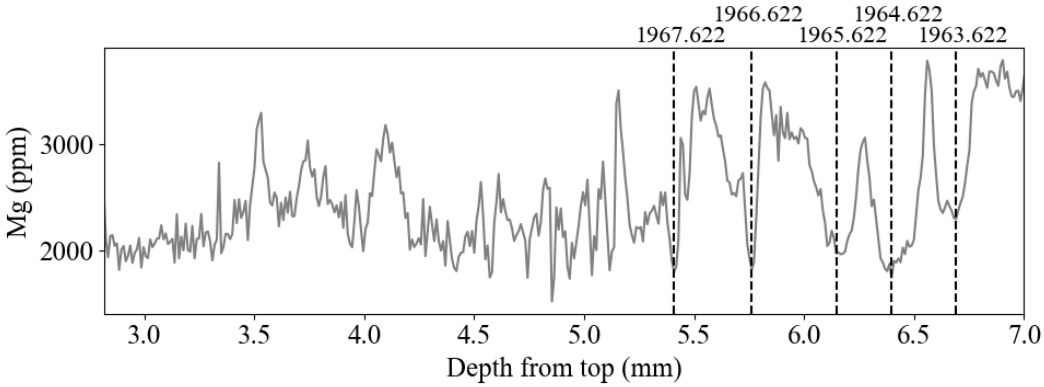

Figure 9: Example of Mg cyclicity. A section of the BER-SWI-13 Mg record with five annual minima marked by the vertical dashed black lines. Note that the section before 5.4 mm is unannotated due to the loss of visible cyclicity.

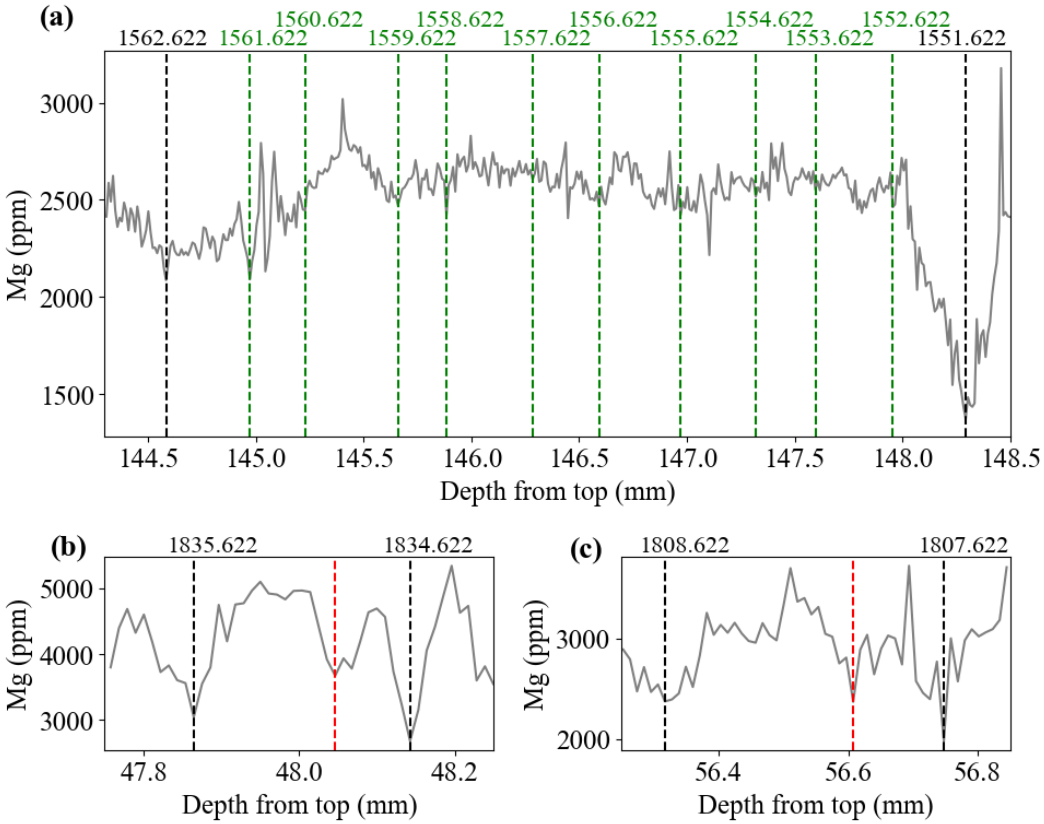

Figure 10: Radiocarbon modelling methodology. (a) a section with indiscernible cyclicity that was modelled to the radiocarbon mean growth rate, where the green vertical lines denote added cycles. Note that added cycles were split equally and adjusted slightly to reflect the shape of the record. (b) and (c) cycles identified in the preliminary cycle count that were removed (red). Cycles were removed if they were ambiguous and uncharacteristically short.

based on the Mg annual cycles was constructed (Figure 8). The cyclicity is ambiguous for some sections of the record; thus, in the final cycle count these sections were modelled using the radiocarbon chronology (Figure 10). The width of the unclear sections was divided by the mean radiocarbon annual growth rate, and then split equally where the shape of record permitted. This modelling reduced the range in cycle length from 10.1–1711.3 μm yr^{-1} to 73.4–939.2 μm yr^{-1} (Figure 11). The final cycle count consists of ~23.3% added cycles, to which depths of 15–60 mm and 95–150 mm were modelled the least and most, respectively.

Mg concentrations in BER-SWI-13 are significantly inversely correlated ($r = -0.51$, $p \ll 0.0001$, $n = 217$) with a previously developed coral Sr/Ca-derived SST record from Bermuda (Goodkin et al., 2008). Because the temperature-dependency of D_{Mg} would produce a positive correlation with ambient temperature, Mg concentrations are not a direct proxy for temperature. A clear inverse relationship exists between SST and wind speed (Figure 12), where colder temperatures are associated with higher wind speeds. The negative correlation with the coral record could therefore be explained by the temperature signal being transferred to the stalagmite via wind speed. Intervals of

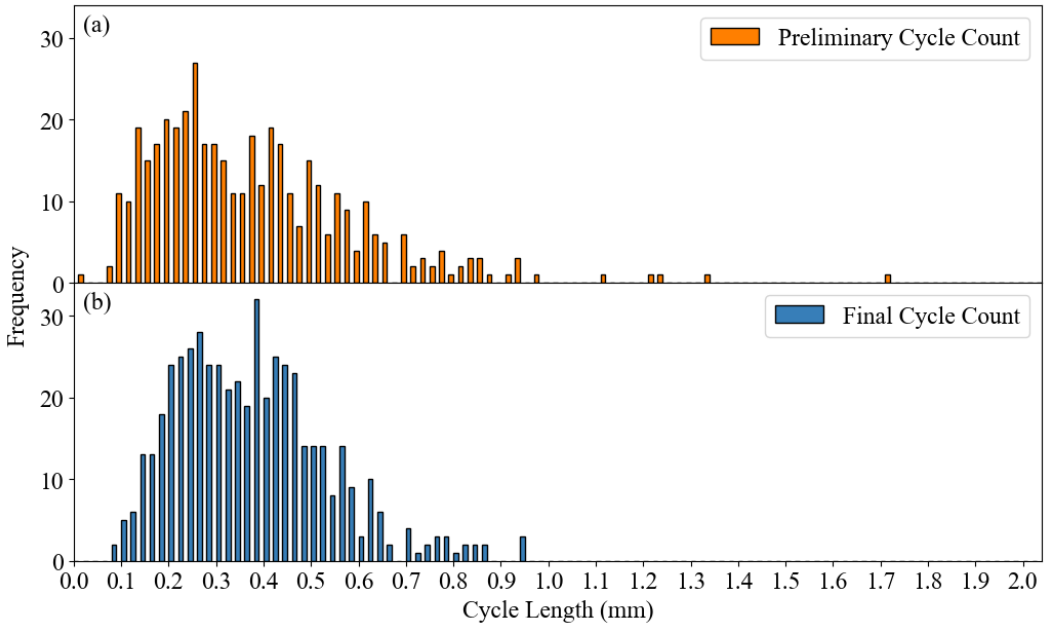

Figure 11: Distribution of annual cycle length for both cycle counts. 'Preliminary' in orange (top panel) and 'Final' in blue (bottom panel).

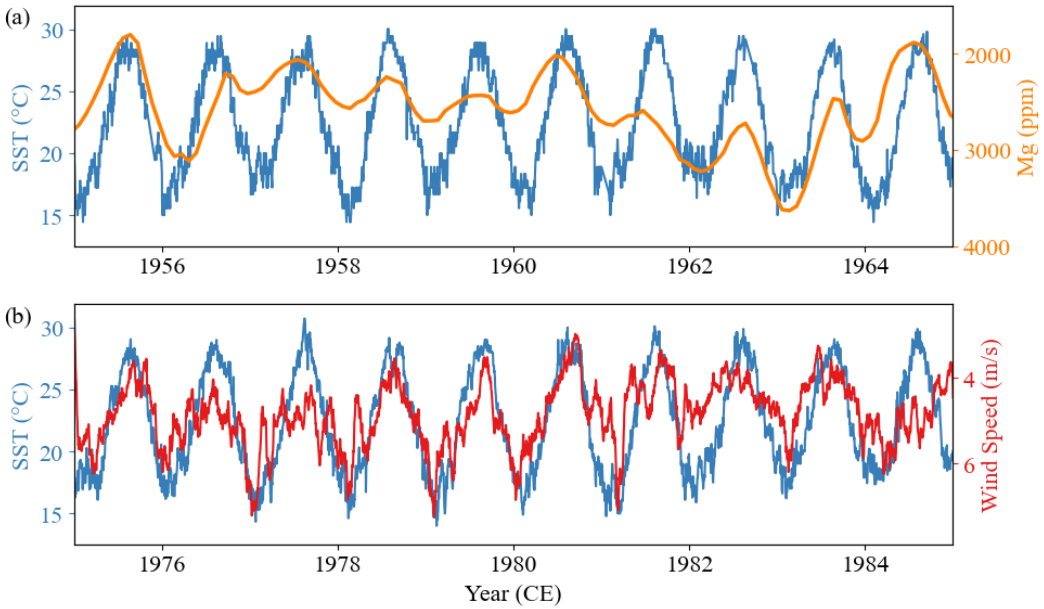

Figure 12: Mg cyclicity shown against SST and wind speed. Mg cyclicity (orange) shown against observational SST data (a, blue) which in turn is plotted against observational wind speed data (b, red) (Bermuda Weather Service, 2018). Mg cyclicity is not directly compared to wind speed variability due to potential anthropogenic impacts on the Mg record post-1970 and wind speed observations beginning in 1975. Note that the Mg and wind speed axes are inverted.

colder temperatures and stronger winds would lead to increased sea spray contributions to rainfall and dripwater, and consequently higher Mg concentrations within the stalagmite due to the higher Mg concentration of seawater. Additionally, because the Mg and Sr data do not plot along a PCP vector (Figure 13), PCP is unlikely to be a significant control on the record. The post-1970 CE data appear to show evidence PCP supporting the view to exclude these data from our interpretations due to alterations to the stalagmite's drip hydrology. However, the Mg and Sr data do plot along a mixing curve between the concentrations of the bedrock and marine aerosols (Figure 13), supporting the perspective that sea spray (in turn controlled by SST) was the dominant control on Mg and Sr concentrations.

By virtue of the apparent inverse relationship between Mg and SST, the Mg cycle count was tuned intra-annually so that the Mg concentration minima were assigned a decimal date corresponding to the 15th of August (midway between the months with

the lowest mean wind speed) and maxima (determined by the broad shape of the cycle rather than local maxima; Figure 14) were assigned a date corresponding to January 1st (start of the month with the highest mean wind speed). The resultant high-precision final cycle count (1456–2013 CE) is consistent with the radiocarbon chronology, with a nearly identical mean growth rate (radiocarbon chronology mean = 344.92 μm yr^{-1}, final cycle count mean = 359.72 μm yr^{-1}; Figure 8c), as well as high intra-annual precision. The final cycle count yields markedly younger values than the U-Th data until ~1580 CE when the U-Th growth rate rapidly increases, whilst also having a

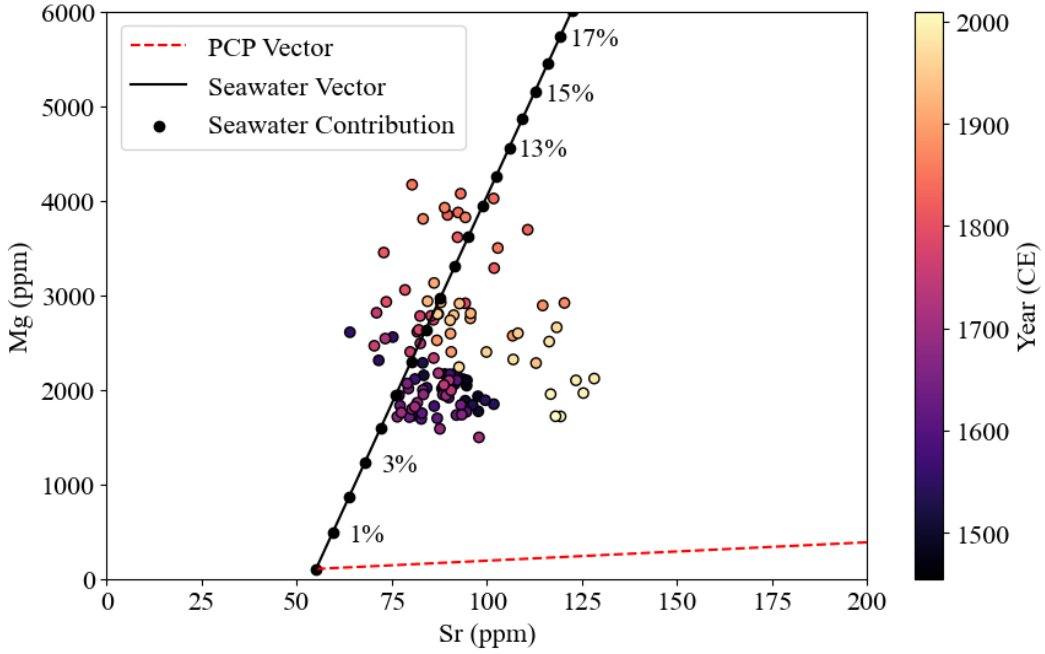

Figure 13: Influence of PCP and seawater on the Mg signal. Five-year binned mean LA-ICP-MS-derived Sr and Mg values for BER-SWI-13 shown against a modelled PCP (dashed red line) and seawater vector (solid black line). The PCP vector was constructed using bedrock concentrations from Rouse (2016) and partition coefficients given in Huang and Fairchild (2001). The modelled seawater vector represents different amounts of marine aerosol contribution to the dripwater and thus resultant calcite (Baldini et al., 2015). 0% marine aerosol contribution is defined as the Mg and Sr concentrations expected in dripwater exclusively from the dissolution of the surrounding bedrock. The percentages (denoted by the grey points on the seawater vector in increments of 1%) represent the addition of a given amount of seawater into the dripwater, where elemental concentrations of seawater are derived from global averages (Chester, 2009).

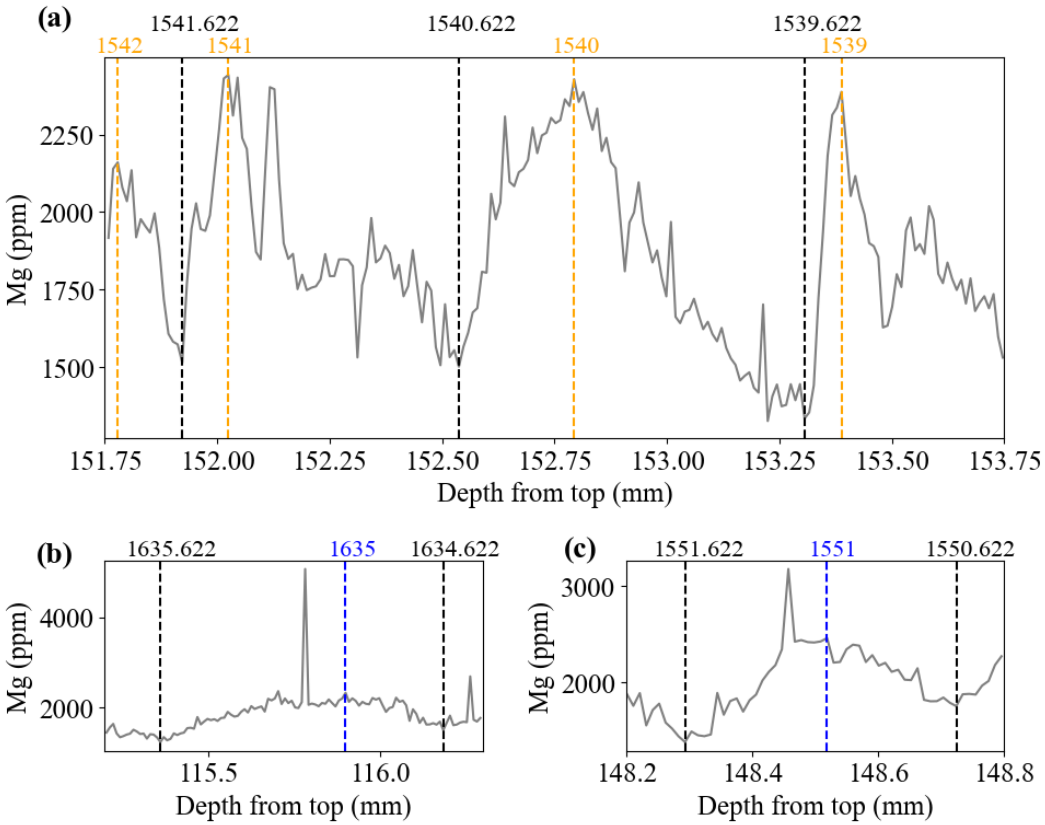

Figure 14: Maxima assignment methodology. (a) a section with clearly defined maxima (orange vertical dashed lines). (b) and (c) examples where the maximum value between two minima likely reflects the influence of an extreme weather event. Hence, maxima (blue vertical dashed lines) are assigned based on the shape of the cycle.

more consistent annual growth rate (range in annual cycle length - final cycle count: 865.8 µm yr^{-1}; U-Th: 1791.8 µm yr^{-1}). The COnstructing Proxy Records from Age models (COPRA) algorithm (Breitenbach et al., 2012) was used to develop an age-depth model with cycle count annual maxima and minima as inputs. The resultant COPRA model incorporated 2000 Monte Carlo simulations and PCHIP interpolation to assign precise ages to every data point. The COPRA algorithm did not identify any hiatuses in the record. The complete dataset consists of 18,471 data points and creates a record of sub-monthly resolution with an average of 33.2 values per year.

4.5 Mg-SST Calibration

The correlation of the Mg record with the SST reconstruction from Goodkin et al. (2008) suggests that a palaeotemperature reconstruction based on the Mg record is viable. This is corroborated by the apparent ocean temperature control on Mg as indicated by observational SST data. To remove the effects of extreme weather events the Mg record was interpolated to monthly spacing and passed through a Savitzky-Golay filter, thus helping to extract the variation attributable to the temperature control.

4.5.1 Dynamic Time Warping

Dynamic time warping (DTW) is a form of time series analysis which applies an algorithm that assesses two or more records for temporal inconsistencies. In palaeoclimatology, it can be used to find an optimal pairing of finite series by applying

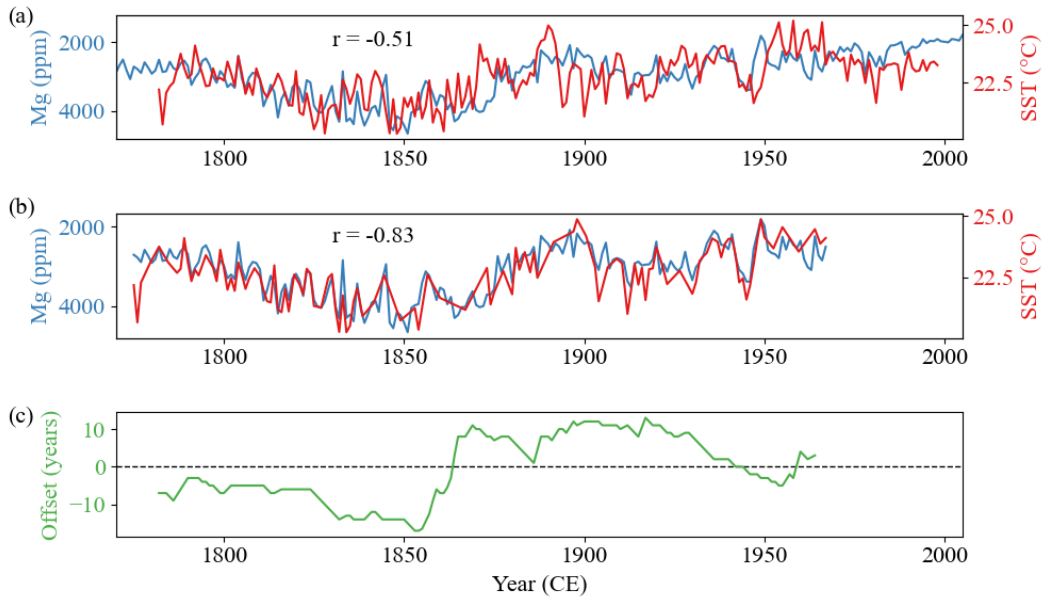

Figure 15: DTW results. (a) The original coralline SST record (red) against the annual magnesium record (blue). (b) The warped coralline SST record (red) against the annual magnesium record (blue). (c) The temporal offset applied to each year.

chronological offsets to a query dataset to maximise its correlation with a reference dataset. To achieve the most accurate temperature estimates possible from the Mg record, the correlation with the SST reconstruction was maximised using dynamic time warping (DTW) within MATLAB (Figure 15). In this case, DTW was used only to derive better temperature estimates and thus the chronology of both records remains unchanged for the analysis. Due to the Goodkin et al. (2008) record's chronology being limited to just a layer count with no statistical approximations for miscounting, it was warped to match the Mg record and account for any chronological discrepancies. A maximum shift of 25 years was also specified to avoid overfitting. Due to the high chronological uncertainty after 1970 CE described in Section 4.4, only the overlap between the records pre-1970 was passed to the DTW algorithm.

The DTW improved the Pearson correlation coefficient (r) by 59% (from r = -0.51 to r = -0.83) by assigning values before (after) 1864 older (younger) ages. The applied temporal offsets ranged from -17 years to 13 years with a mean of -0.6 years. The DTW suggested that the ages given to the SST record pre-1864 were too young, indicating an undercount. Goodkin et al. (2008) speculated that undercounting bias would be most prevalent in in the early to mid-1800s when growth rates were extremely slow, and this is confirmed by the DTW offset applied during this period. Additionally, the implied overcount in the younger half of the SST record may be due to noise in the Sr/Ca or annual band data leading to cycle misidentification (Goodkin et al., 2008).

4.5.2 Mg-SST Model

The data appear to have a 2nd order polynomial spread in Mg-SST space. However, initial modelling found the quadratic term to be very small (4.305×10^{-8}) and not statistically significant ($p = 0.65$). To confirm the choice to remove the term, a test for multicollinearity was performed. This determines whether predictor variables are correlated by calculating the Variance Inflation Factor (VIF). VIF is a measure of how much collinearity inflates the variance of estimated regression coefficients, where

values over 10 are diagnostic of substantial multicollinearity. The test indicates very high multicollinearity is present between the linear and quadratic terms (VIF = 87.14). Therefore, statistical modelling does not support the extra complexity, and so further modelling assumes linearity.

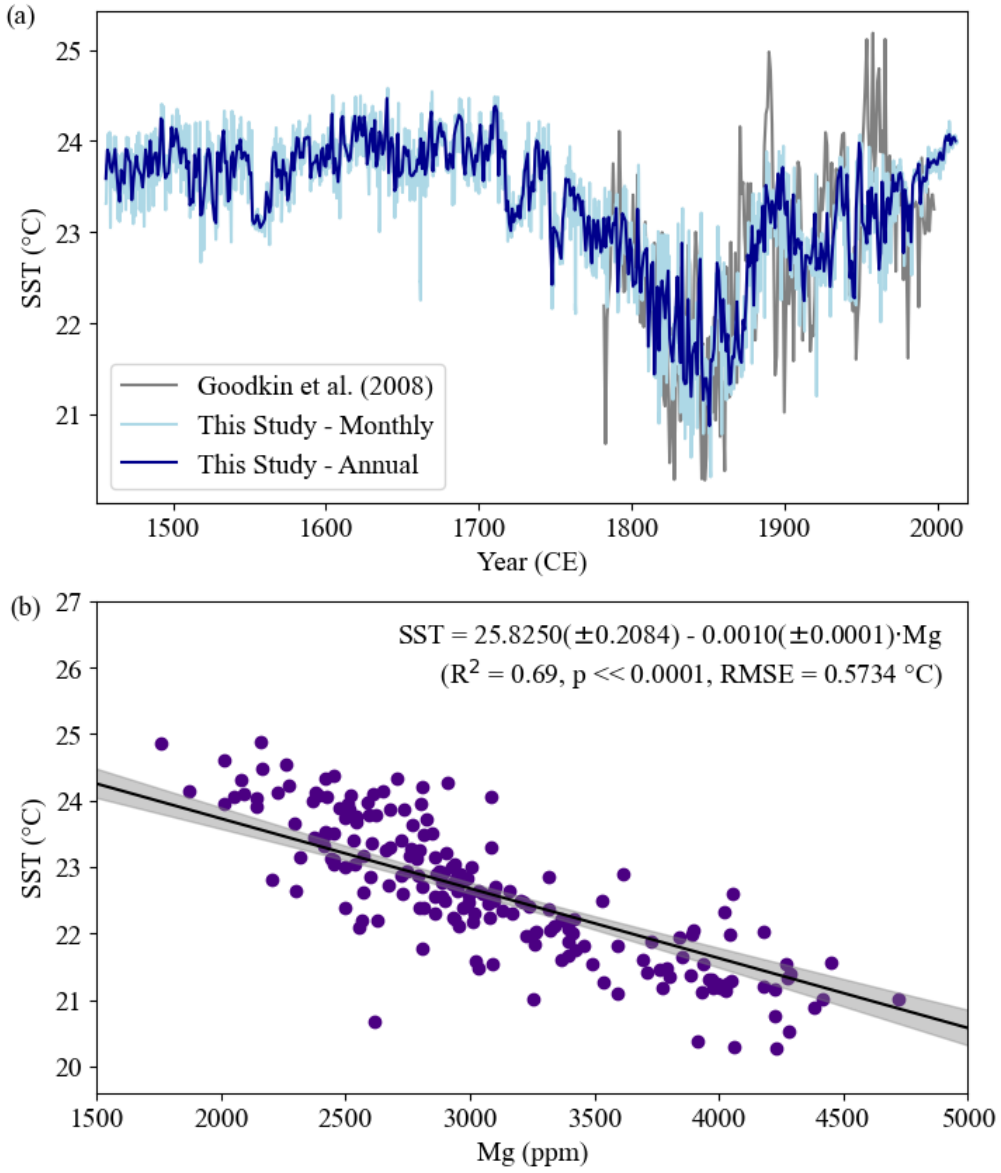

Figure 16: SST model output. (a) Cochrane-Orcutt regression model output (1456–2013 CE; 558 years) at both a monthly (light blue) and annual (dark blue) resolution plotted with a coralline SST record (1782–1998 AD; 217 years) for Bermuda (Goodkin et al., 2008). (b) warped 1782–1964 coralline SSTs regressed against stalagmite Mg concentrations.

An initial ordinary least squares (OLS) regression between the Mg values, with a growth rate correction term, and the warped SST values returned a high correlation coefficient (R^2 = 0.69, p ≪ 0.0001, n = 193). However, this regression found the growth rate term to be non-statistically significant (p = 0.29) and the residuals to be autocorrelated (DW = 0.95), indicating that part of the relationship between Mg and SST was not being captured. Thus, the regression was corrected using a Cochrane-Orcutt estimation to include an AR(1) term and the growth rate term was removed (Cochrane and Orcutt, 1949). The final linear regression yielded the following correlation (Figure 16b):

$$SST = 25.8250(\pm 0.2084) - 0.0010(\pm 0.0001) \cdot Mg$$
$$(2\sigma, 95\%\ conf., R^2 = 0.69, p \ll 0.0001, RMSE = 0.5734°C)$$

The model's strong correlation coefficient and low error term values suggest the corrected model performs well. Additionally, the modelled stalagmite SST record has less variance than the coralline record, likely because of aquifer mixing smoothing the signal somewhat (potentially the mixing of diffuse and concentrated flow paths).

4.5.3 Model Validation

The regression's predictive power was evaluated using split-period calibration/verification tests in both directions (Figure 17), which involved dividing the record into two halves and testing the modelled temperature estimates against the Goodkin et al. (2008) SST values. To quantify the model's skill, the following statistics were used in addition to Pearson correlation coefficient (r) and R square (R^2):

- **Durbin-Watson (DW)**

  A statistic ranging from 0 to 4 which indicates the presence of lag-1 autocorrelation in the residuals of a regression. Values close to 2 indicate no statistical evidence of residual autocorrelation, while lower (higher) values provide evidence of positive (negative) autocorrelation. Autocorrelated residuals violate the assumption of independence in an OLS regression and

indicate a significant proportion of the relationship between the regressed variables is not being captured.

- **Reduction of Error (RE)**

  A highly sensitive statistic that checks whether the model performs better than the mean of the calibration period. It ranges from negative infinity to 1, where a positive value indicates that the model has skill (Cook and Kairiukstis, 2013).

- **Coefficient of Efficiency (CE)**

  This metric is very similar to RE; however, it compares the model to the mean of the verification period. Its interpretation is the same as that of RE.

- **Signs Test (ST)**

  A non-parametric measurement of reliability that counts the number of times that excursions from the mean in the model agree with those of the target dataset (Cook and Kairiukstis, 2013). While there is a critical value, it is usually reported as the number of agreements followed by the number of disagreements.

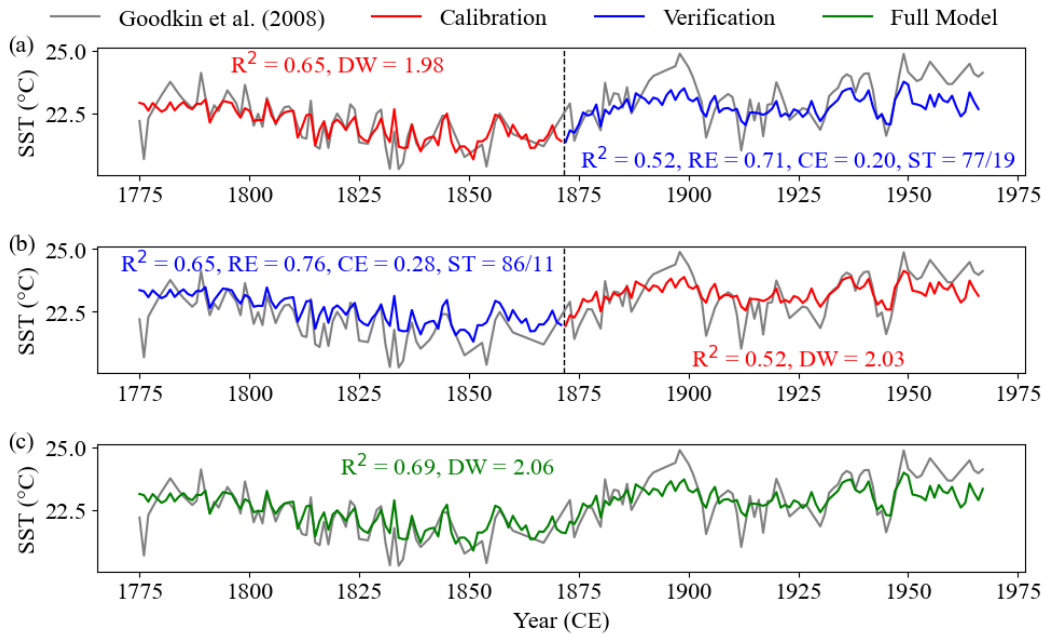

Figure 17: Split-period testing of the Cochrane-Orcutt regression. The forward (a), reverse (b), and full (c) model results. DW - Durbin-Watson statistic; RE - reduction of error statistic; CE - coefficient of efficiency statistic; ST - signs test.

Overall, the model passed the tests on every metric. Interestingly the backward model performed better than the forward model, but this is likely due to the prolonged positive excursion in the target SST record in the late 1800s not being present in the Mg-derived reconstruction. The full model showed no residual autocorrelation and returned low error term values (RMSE = 0.57°C, MAE = 0.43°C, MAPE = 1.90%). Thus, the final model described in Section 4.5.2 has significant predictive power and appears to yield accurate SST estimates.

4.6 CHANGEPOINT ANALYSIS

Changepoint analysis is a statistical technique that identifies instances where the stochasticity of a time series changes. The changepoint algorithm can look for changes in the mean, variance, correlation, spectral density, or even a combination of measures. This type of analysis is used to detect tipping points in palaeoclimate records (e.g., Bhatta et al., 2023; Duesing et al., 2021; Trauth et al., 2018). For example, Trauth et al. (2018) used changepoint analysis on a lake sediment record from southern Ethiopia to determine the amplitude and duration of past climate transitions, including the onset of the African Humid Period (AHP) ~15,500 years BP. However, its use in the field of palaeoclimatology is limited as it is still a moderately new technique.

This thesis uses the R package Rbeast, which uses a Bayesian model averaging algorithm called BEAST to decompose a given time series into individual components (Zhao et al., 2019). By using Bayesian statistics (a branch of statistics that uses probability distributions to model uncertainty and make inferences), the package is not only able to identify changepoints but also quantify the probability of changepoint occurrence over time. Here it is used to detect statistically significant deviations from pre-industrial levels in a variety of different AMOC reconstructions.

5 Results and Discussion

5.1 Bermudan Temperature Trends

The resultant stalagmite-derived SST reconstruction exhibits notable agreement with both five previous coralline palaeotemperature records from offshore Bermuda (Draschba et al., 2000; Goodkin et al., 2008; Kuhnert et al., 2002) and reanalysis data (Rayner et al., 2003), illustrating its reconstructive power (Figure 18). The record

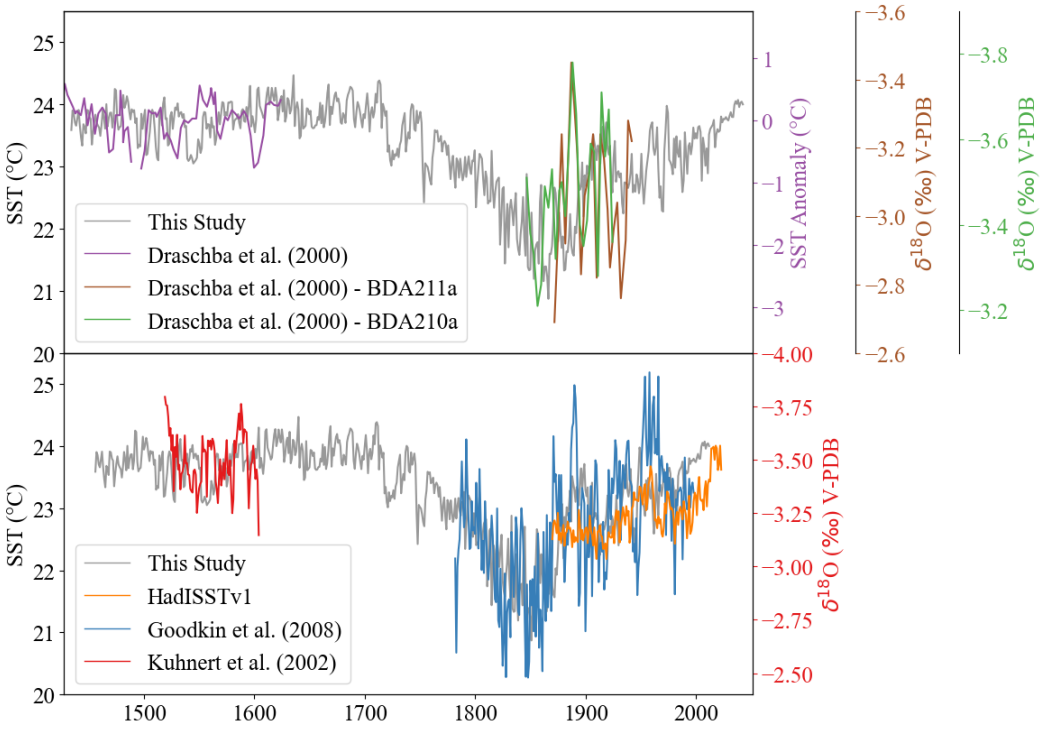

Figure 18: Comparison with other Bermuda SST records. The stalagmite-derived SST reconstruction presented here (grey) against five coralline palaeo-ocean temperature records for Bermuda, as well as a reanalysis record (HadISSTv1) for the region (resolution = 1° × 1°, Rayner et al., 2003). Note that the Kuhnert et al. (2002) record was averaged to annual spacing to reduce noise and that axes have been inverted to match the direction of the SST axis, which the reanalysis and Goodkin et al. (2008) records are both plotted against.

presented here cannot confidently be compared to observational SST data due to anthropogenic influences post-1970 (see Section 4.4) and observations starting in 1950. However, because the Goodkin et al. (2008) record is derived from a regression with instrumental data, its correlation with the stalagmite reconstruction reinforces the accuracy of the record. Although the lower frequency variability of all six reconstructions shows strong agreement, the annual scale variability is not as consistent between records. This could be due to many potential reasons including localised factors (such as exact weather patterns or microclimates altering the signal), differences due to archive type (for example terrestrial archives likely having a greater propensity to record shorter-scale atmospheric variability), chronological uncertainties, limitations associated with the proxy, or instrumental errors incurred through data collection. Additionally, the lower variance in the reconstruction presented here may be more accurate than thought in Section 4.5.2 because both reanalysis and observational data show less variance than the coralline record. The records

The new stalagmite SST record (Figure 18) suggests that SSTs prior to the start of the 1700s were largely stable, with a range of 1.4°C about a mean value of 23.8°C (1950–2018 average: 22.7°C; Bermuda Weather Service, 2018). A cooling trend lasting ~130 years then ensued from ca. 1720 CE at a rate of approximately -0.13°C per decade and ended with the onset of the warming seen post-1850. The cooling period exhibits high frequency interannual fluctuations with decadal-scale variances on the order of ~1.5°C, compared with less than 0.5°C in the same timescale for the period before 1720 CE. The interannual variance also decreases after 1967, but this is likely the product of hydrological changes at the site rather than changes in climate as the annual signal across that interval is also less pronounced, despite no change in the annual climate signal. Both reconstructions indicate a warming of ~0.96°C per 100 years starting around 1850 CE. The records also both suggest a brief cooling interval starting in the late 1800s which lasted around two decades before warming resumed.

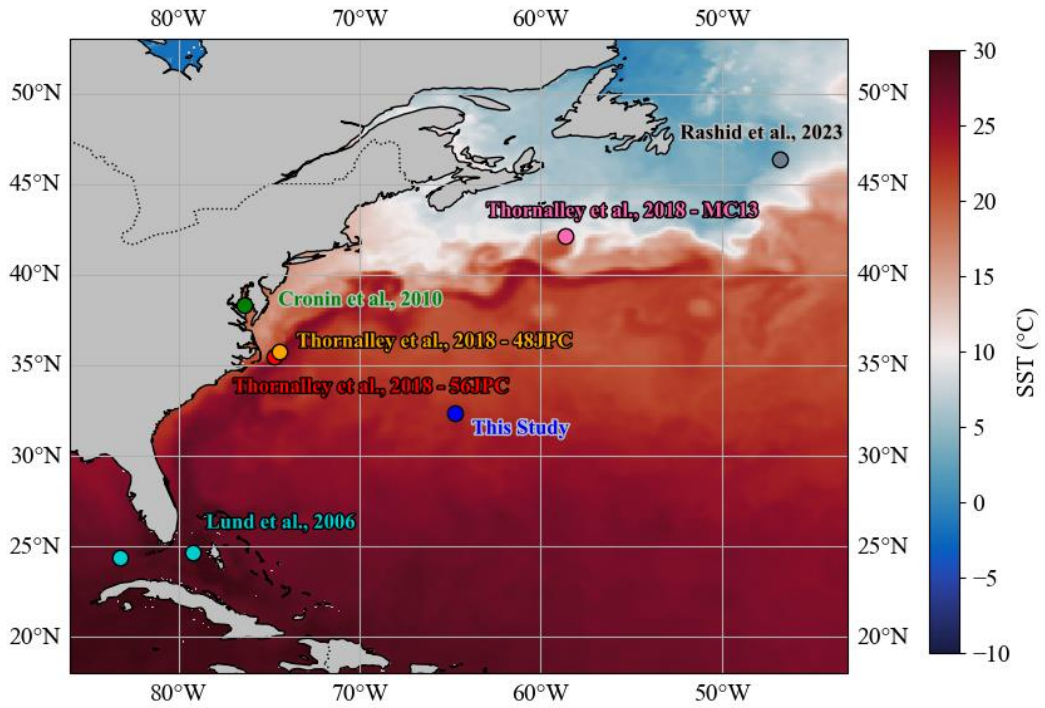

Figure 19: Map of North Atlantic regional SSTs. Coloured circles denote the sites of the records in the Figure 20. SST data from Copernicus Marine Service (2024).

5.2 Influences on Reconstructed SST Variability

The SST record reconstructed here likely exhibits the effects of both changes in ocean currents and anthropogenic climate change. Enhanced radiative forcing from additional greenhouse gases and rising total solar irradiance at the end of the LIA likely explain the increase in temperatures seen after 1850 CE (Figure 20a and 20g). Although, despite Northern Hemisphere temperature anomalies being largely low before the mid-1800s (Figure 20g), reconstructed Bermudan SSTs show unusually high temperatures pre-1700 CE.

N. pachyderma abundances in a sediment core from the northwest Atlantic also suggest a warming trend beginning in the 1700s (Figure 20a). Similarly, a Mg/Ca-derived temperature record for Chesapeake Bay demonstrates moderate SSTs during

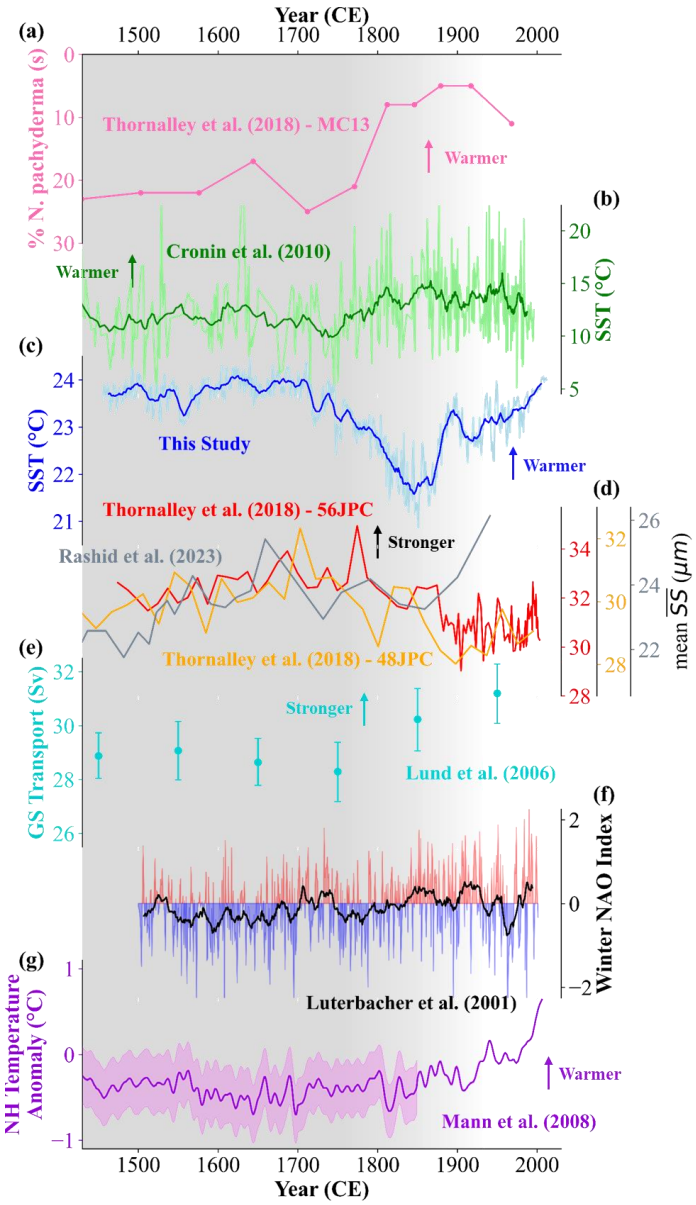

Figure 20: Palaeoclimatic records for the time interval. (a) Percentage abundance of the polar species N. pachyderma (sinistral) in a marine sediment core (OCE326-MC13) from the Northwest Atlantic (Thornalley et al., 2018). (b) Chesapeake Bay reconstructed SST data with a 15-point moving average (Cronin et al., 2010). (c) The annual SST model for Bermuda with a 15-point moving average. (d) Mean sortable silt ($\overline{SS}$) grain size data from three cores (red, 56JPC; orange, 48JPC; grey, MO217) (Rashid et al., 2023; Thornalley et al., 2018). (e) Gulf Stream transport estimates in the Florida Straits (Lund et al., 2006). (f) Normalized winter North Atlantic Oscillation index data with 15-point moving average (Luterbacher et al., 2001). (g) Northern Hemisphere temperature anomaly reconstruction with 95% confidence interval for proxy-derived estimates (Mann et al., 2008). Grey area denotes temporal extent of the LIA.

the LIA before beginning to increase in the mid-1700s (Figure 20b). However, our Bermuda record (Figure 20c) suggests regional ocean temperatures were high during the oldest part of the record until a cooling trend ensued around 1720 CE lasting approximately 130 years. The opposing temperature trends suggest a 'thermal seesaw' between the records, whereby an increase in SSTs at lower latitudes leads to a decrease at higher latitudes. This probably reflects GS migration south during the LIA causing the observed rise in regional Bermudan SSTs compared to those seen at higher latitudes. We propose that a combination of weakened transport, a stronger LC and DWBC, and a sustained negative North Atlantic Oscillation (NAO) phase caused the GS separation point to shift south during the LIA, possibly reducing subtropical mode water potential vorticity. Keigwin and Pickart (1999) suggested that northward slope water current migration during the LIA was responsible for an observed warming in several cores south of Newfoundland, but our SST record indicates a broader antiphase system suggesting the northward ocean current shift was more widespread.

GS, DWBC and LC flow-speed reconstructions further support this proposed GS drift (Figure 20d-e). Thornalley et al. (2018) showed the DWBC was stronger towards the end of the LIA using two mean sortable silt ($\overline{SS}$) records from sediment cores off Cape Hatteras (Figure 20d). A DWBC weakening from about 1750 CE also supports the notion of a northward shift in the GS separation point starting around the time. Rashid et al. (2023) found the LC to be strongest during the LIA (over the last 1.45 ka) using $\overline{SS}$ data from a core off the southeastern Grand Banks (Figure 20d), which would also have caused the GS to separate from the coast further south (Joyce et al., 2019; Sanchez-Franks et al., 2016; Taylor and Stepens, 1998; Thibodeau et al., 2018). Lund et al. (2006) reconstructed Florida Current transport over the last millennium using sediment cores near the Dry Tortugas and Great Bahama Bank (Figure 20e). From this reconstruction they estimate that the GS was systematically weaker during the LIA by approximately 10%, which given the stronger subpolar gyre at the time implies that the GS would have moved south at the time and reduced northward heat transport (Thibodeau et al., 2018).

Furthermore, studies have also found a link between the GS and the NAO, an atmospheric circulation phenomenon associated with changes in the surface westerlies across the North Atlantic (Taylor and Stepens, 1998). The NAO index is defined by the normalised pressure difference between the Icelandic Low and the Azores High and modulates mid-latitude westerly strength as well as heat, freshwater, and momentum fluxes in the North Atlantic (e.g., McCarthy et al., 2018; Zhang et al., 2020). Studies have linked the NAO to changes in both North Atlantic Deep Water (NADW) formation and Labrador Sea convection (Zhang et al., 2020). During a more negative NAO phase, decreased heat loss, more precipitation, and weaker winds reduces convection in the Labrador Sea, corresponding to a weaker AMOC and in turn a more southerly GS path (Medhaug et al., 2012). This is evident in current GS path migration (1993–2016), which may reflect an increasingly negative NAO (e.g., Chaudhuri et al., 2011; Taylor and Stepens, 1998). Hence, the persistent negative NAO index values pre-1700 observed in the Luterbacher et al. (2001) winter NAO reconstruction also corroborate a southward GS during the LIA (Figure 20f).

The low Mg concentrations pre-1700 in Bermuda may be also attributable to weaker westerlies during the extended negative NAO phase. A weakening of the westerlies at this time could have reduced sea spray over the site and thus led to less Mg incorporation into the stalagmite. These weaker winds are evident in the relatively low implied seawater contribution from the Mg and Sr concentrations at the time (~4.97% compared to the mean ~6.10%; Figure 13). Considering that a transition in the 1700s can also be seen in sediment core-derived temperature and flow speed reconstructions (e.g., Cronin et al., 2010; Thornalley et al., 2018) there is likely a direct temperature effect in addition to any changes in wind speed. Thus, the GS likely did migrate at this time, but the potential for reduced wind speed over Bermuda to exaggerate the reconstructed SST signal complicates the quantification of the exact southward positional extent of the GS movement. Furthermore, a change in cave processes (such as degree of WRI or PCP) is unlikely to be the primary driver of Mg concentration variability as they are controlled by broader climatic factors, and only the period after 1967 exhibits the effects of PCP (Figure 13). For this reason, although cave processes

may reduce the accuracy of the temperature estimates, the trends exhibited here are likely not exclusive to the BER-SWI-13 record and reflect broader regional trends.

Assuming our SST estimates reflect exclusively temperature change without amplification due to wind speed, the 1–2°C temperature change over 130 years suggests a moderately fast rate of GS migration when considering the relatively flat nearby SST gradient in the modern North Atlantic (Figure 19), implying that GS position is reasonably sensitive to forcing. Observational data tracking the current northward GS migration detected a shift in the Gulf Stream North Wall of ~1.5° in 52 years (1965–2017) between 50°W and 40°W (Seidov et al., 2019). Therefore, with the continuation of current trends in the GS and AMOC, the sensitivity of regional temperatures to GS path drift could have serious ramifications for future regional climates, ecosystems, and extreme weather events.

5.3 NAO SIGNAL

In addition to the GS-NAO link explained in the previous section, the cyclicity present in the record (Figure 20c) when compared to the smoothed NAO reconstruction (Figure 20f) highlights its influence on shorter timescales.

The pressure difference between the Icelandic Low and the Azores High known as the NAO is responsible for climate variability across the North Atlantic through atmospheric dynamics. When both pressure centres are stronger than average there is a larger difference, indicative of a positive NAO phase. During a positive phase the increased pressure difference results in a northward shift of the storm track and a stronger Atlantic jet stream. Thus, there is more sea spray over the site and hence higher Mg incorporation into the stalagmite meaning reconstructed SSTs are lower. The NAO exhibits notable cyclical behaviours on interannual to multi-decadal timescales through its teleconnections with other climate mechanisms (Seip et al., 2019). Studies have attributed a variety of periodicity bands to the influence of the

NAO, including: 7–9 years, 13 years, 16 years, 20 years, 26–27 years, and 34–36 years (Seip et al., 2019).

The detrended SST reconstruction is consistent with the Luterbacher et al. (2001) NAO record (Figure 21a; r = -0.20). Post-1820 the two records are in-phase and match at interannual resolution. However, before this date the SST record becomes increasingly out of sync with the NAO index. By translating the shape of the SST record across to the NAO index, it suggests there is a series of undercounts in the stalagmite's chronology. The records are 15–16 years adrift in the early 1700s and 22–24 years out of phase in the late 1500s. This implies there is a 15–16-year undercount in the late 1700s and an additional 7–9 missing cycles in the mid 1600s. The alignment when considering these additional cycles, suggests potential overcounts in both the late 1600s and mid 1500s. Both overcount intervals correspond to areas of the cycle count that were modelled to the radiocarbon chronology, and thus have a higher propensity for overcounting. All the shifts mentioned above amount to a total error of

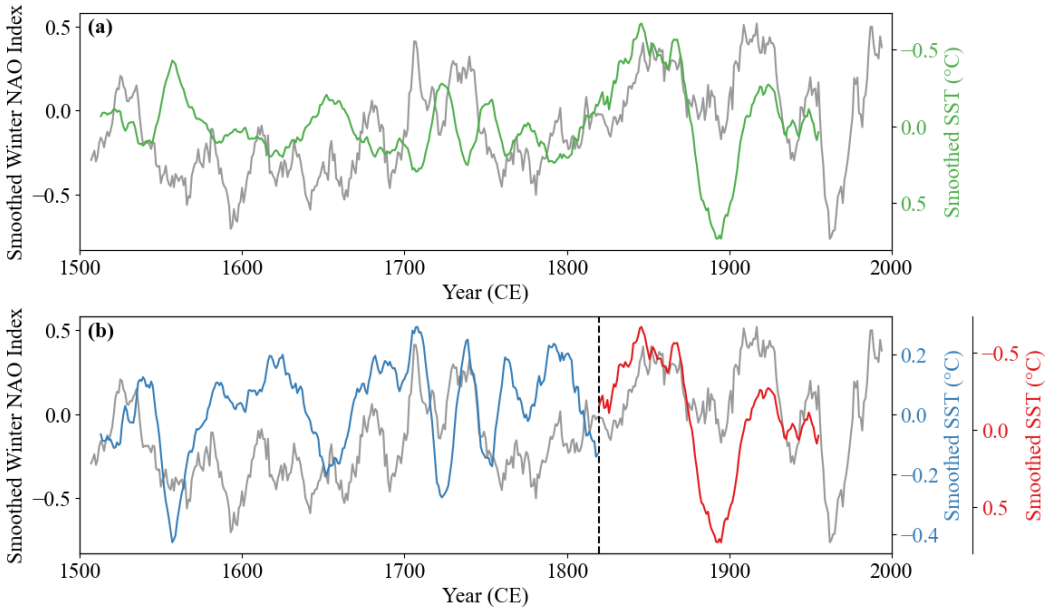

Figure 21: NAO signal in the Bermuda reconstruction. (a) Normalized winter North Atlantic Oscillation index data (grey) shown with the stalagmite SST record (detrended using a 101-pt moving average), both smoothed with a 15-pt moving average. (b) same as (a) but split at 1820 CE (black vertical dashed line) and plotted on axes of opposing directions.

~25 years and so are within chronological uncertainties. However, the mismatch is also approximately half the periodicity of many NAO cycles, suggesting a potential anti-phase relationship. Splitting the SST reconstruction at 1820 CE (Figure 21b) yields a negative correlation (r = -0.42) in the younger section and a positive correlation in the older section (r = 0.23). This reversal could be the result of anthropogenic influences on atmospheric circulation causing the relationship described above. However, a reversal is not discussed in the literature and so an undercount may be more likely.

5.4 WIDER IMPLICATIONS

5.4.1 Gulf Stream Variability

One method to assess GS variability is to use indices, which help to monitor GS state whilst being readily interpretable. The most common uses the number of degrees latitude the position of the GS deviates from the average. A different example is presented in Caesar et al. (2018). Their index is defined by the region in the western Atlantic Ocean demonstrating above-average long-term warming due to the AMOC slowdown. Hence, it reflects SST change in the GS region instead of directly quantifying GS transport. The record spans 146 years (1871-2016) and is derived from reanalysis data (HadISST).

The stalagmite SST record exhibits a significant correlation with the GS index from Caesar et al. (2018) (Figure 22; r = 0.59, $p \ll 0.0001$, n = 132). However, there is a slight misalignment between the two records which likely arose due to the chronological uncertainties in both records. Accounting for this by applying a 5-year shift to the GS index, the correlation coefficient rises to r = 0.69. Despite the high degree of chronological uncertainty post-1970 in the Bermuda reconstruction, the two records exhibit similar trends and appear to be in-phase at lower-frequencies. The disparities between the two records at higher-frequencies may be due to a variety of

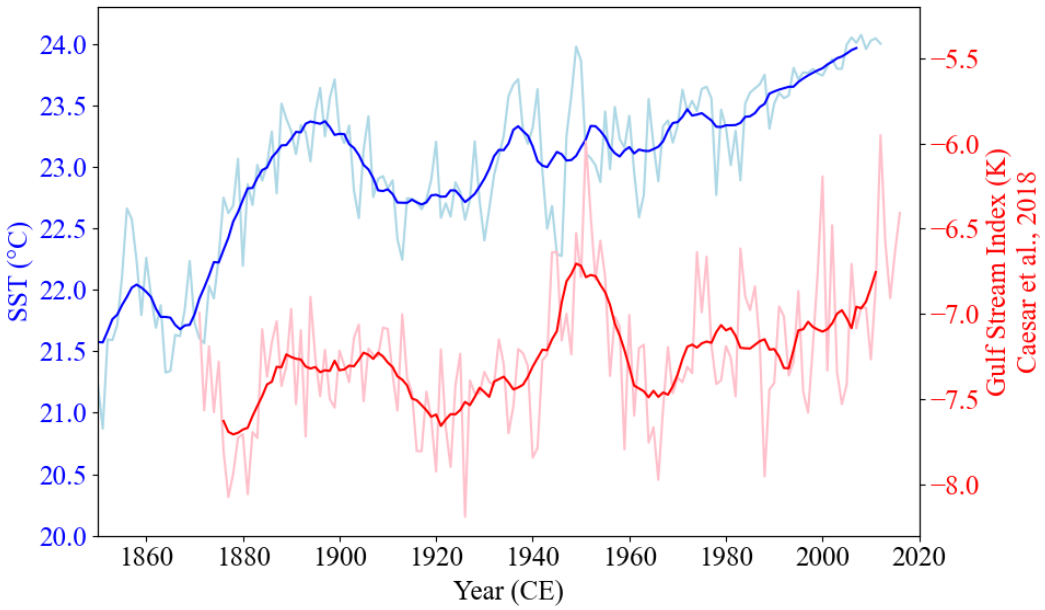

Figure 22: Comparison with a reanalysis Gulf Stream index. Blue (top) is the reconstructed Bermudan SSTs presented here. Red (bottom) is the HadISST-derived Gulf Stream Index from Caesar et al. (2018). Dark blue/red lines show 11-pt moving averages.

reasons, including: (1) additional SST forcing besides the GS in the Bermuda record, (2) the compounding effects of wind speed on the Bermuda record, (3) localised effects on the SST signal, or (4) chronological uncertainty.

The notable agreement between these two records reconfirms the accuracy of the SST reconstruction and potentially the link to the GS. Therefore, although the SST reconstruction presented here is not a direct GS index, this correlation provides evidence for its use as an indicator of long-term GS variability and supports the findings discussed in Section 5.2.

5.4.2 AMOC Weakening

Because of the link between GS position and AMOC strength, the Bermuda reconstruction from this study may be able to provide insights into AMOC strength as well. Modern AMOC weakening is broadly accepted to have started in the mid-1800s and accelerated in the mid-1900s (e.g., Caesar et al., 2021). However, if the change in

GS position in the early 1700s (discussed in Section 5.2.) is indicative of a more widespread weakening, then modern AMOC decline could have begun over a century earlier.

Changepoint analysis is a technique to reveal statistically significant deviations from the mean and/or change in variance in a time-series. This analysis finds three significant changepoints in the Bermuda record: 1593, 1722, and 1917 (Figure 23). The same method finds early 1700s changepoints in two of four AMOC indices

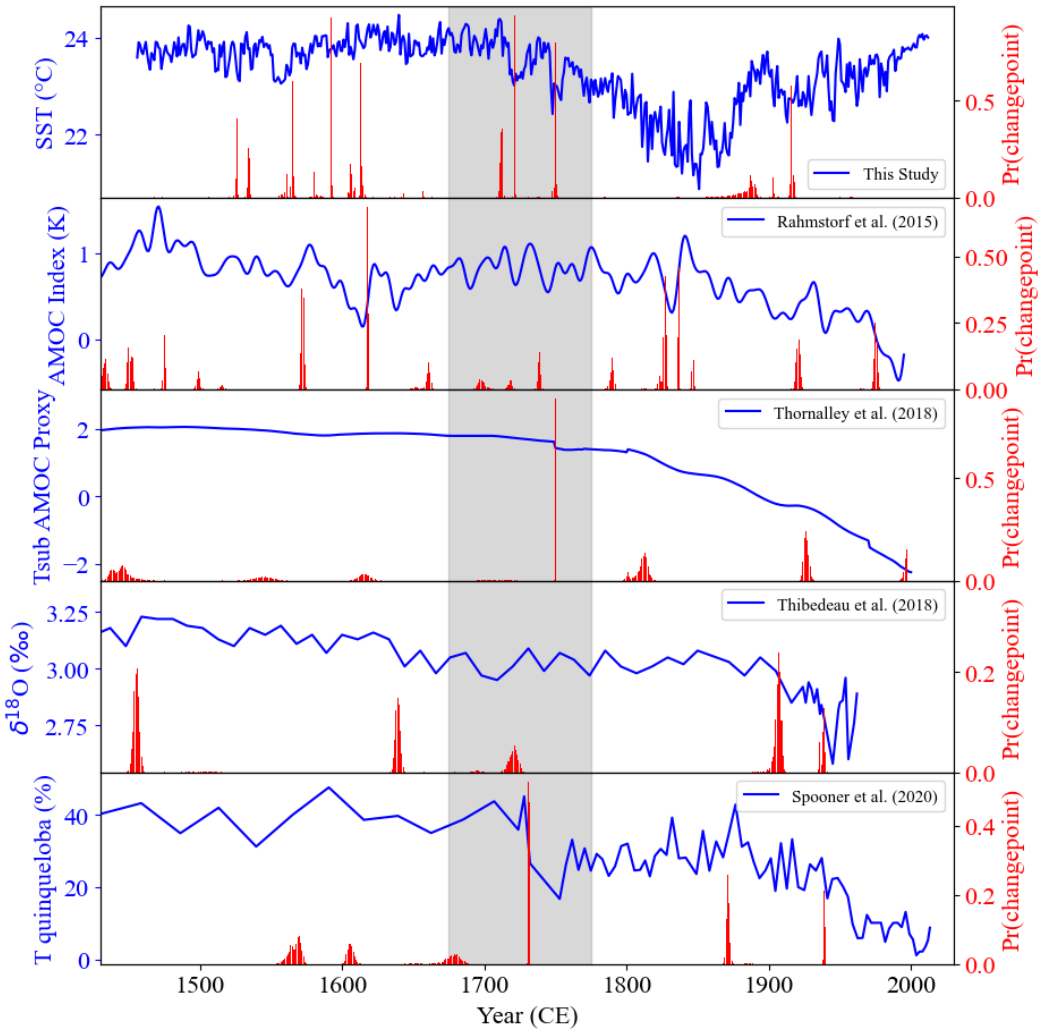

Figure 23: Changepoint analysis results. Top is the Bermuda record from this study followed by four AMOC indices that span the same time interval. Blue lines denote the record. Red bars show the statistical likelihood of a changepoint at a given time. The grey area highlights the potential early 1700s decline.

(namely Spooner et al., 2020; Thornalley et al., 2018), which were chosen because they spanned more than the last three centuries. The absence of a significant changepoint at this time in the other two records may be due to the method by which the AMOC fingerprint is derived. Rahmstorf et al. (2015) use the difference in temperature anomaly between the subpolar gyre region and the Northern Hemisphere average to construct their record. Similarly, Thibodeau et al. (2018) use a sediment core from the Gulf of St. Lawrence. Due to both method's chosen localities, a smaller scale regional weakening may be lost in these records. Both Thornalley et al. (2018) and Spooner et al. (2020) use cores from the mid-Atlantic and so may sample a different section of the AMOC. Therefore, modern AMOC weakening may have started in the early 1700s following freshwater release with the abatement of the LIA, followed by further steep weakening events in the 1850s and 1950s in response to anthropogenic global warming. If this earlier weakening is indeed diagnostic of broader AMOC decline, it likely implies the AMOC system is more responsive to forcing than previously thought and thus predictions of the proximity of the system to collapse may be underestimated.

5.4.3 Areas for Future Research

Further research should focus on the following aspects of the material presented here:

- **Compounding Wind Factor**
  A method to determine the degree of wind contribution to each SST estimate would help in understanding the accuracy of the model as well as the conclusions from it regarding ocean circulation change. Although there is a connection between temperature and wind so conclusions are unlikely to be changed, it may help to constrain exact degrees of GS positional change.
- **Influences From Other Oscillations**
  Understanding the contribution of climate phenomena such as the NAO, AMO, and ENSO will provide a way to potentially extract reconstructions of these

oscillations. In the case of the ENSO, it may also offer a unique insight into the teleconnection between the Pacific and North Atlantic climates.

- **Early 1700s Decline**

  Further analysis of true AMOC indices into the presence of an early 1700s weakening will help to understand whether this event was indeed widespread or localised to the GS region. Also, it will aid predictions of future AMOC state and sensitivity.

- **AMOC Future**

  Although less directly related to this study, substantial further research is needed to fully understand when the AMOC will collapse, what emissions pathways may avoid a collapse, the implications of a collapse, and thus how to adapt to them.

6 CONCLUSIONS

The recent suggestions of terrestrial stalagmite Mg concentrations as a means to capture changes in ocean temperatures through sea spray contributions to calcite (e.g., Baldini et al., 2015; Sinclair et al., 2012) inspired the use of BER-SWI-13 as an oceanic palaeotemperature archive. This motive was substantiated by a strong significant correlation ($r = -0.51$, $p \ll 0.0001$, $n = 217$) between the derived Mg record and a previously published coralline SST reconstruction, Goodkin et al. (2008). The negative correlation means that Mg is not a direct proxy for temperature but instead an indirect proxy via sea spray contributions to the dripwater feeding the stalagmite. Bermuda's position within the Northwest Atlantic, close to major currents such as the GS highlights its ability to potentially record changes in ocean current strength or position due to its association with SST changes. Climate reconstructions inferring AMOC strength are vital in understanding its sensitivity to future climate change.

The chronology for BER-SWI-13 was modified from the U-Th-derived COPRA age-depth model due to the highly variable growth rate it indicated. For this reason, an updated Mg geochemical cycle count was performed where sections with ambiguous cyclicity or extreme growth rates were modelled to a calculated radiocarbon mean growth rate. The resultant chronological model utilises 1955 and 2013 CE anchors and counts 558 annual cycles meaning the record spans the time 1456–2013 CE.

Using the Mg-SST correlation, the Goodkin et al. (2008) coralline SST record underwent DTW to account for chronological offsets and the Mg record was modelled to the warped data with a Cochrane-Orcutt regression. The regression yields accurate SST estimates ($R^2 = 0.69$, $DW = 2.12$, $RMSE = 0.57°C$) for Bermuda spanning more than five centuries. The new SST record consists of three key trends: (1) consistent high temperatures before the early 1700s; (2) intense cooling lasting from the early 1700s to the mid-1800s; and (3) a warming trend after the 1850s.

Similar reconstructions from Chesapeake Bay and the Northwestern Atlantic (off the coast of Nova Scotia) suggest that ocean temperatures were cooler during the LIA followed by a warming trend starting in the 1700s, opposing the elevated SSTs and cooling trend observed in Bermuda (Cronin et al., 2010; Thornalley et al., 2018). This 'thermal seesaw' or dipole pattern suggests that the GS migrated northwards at the end of the LIA following a period characterised by a southern GS path.

Flow speed reconstructions for the GS, DWBC and LC support this interpretation (Lund et al., 2006; Rashid et al., 2023; Thornalley et al., 2018), providing evidence of weakening southward currents in the 1700s from strong conditions during the LIA. Additionally, multiple AMOC indices find significant changepoints in the early 1700s suggesting that the GS path migration may be part of a broader AMOC weakening. Current understanding finds two onsets of AMOC weakening in the Common Era: (1) the mid-1800s likely due to enhanced freshwater fluxes from the Arctic and Nordic seas (Thornalley et al., 2018); and (2) the mid-1900s likely because of anthropogenic warming (Caesar et al., 2018). This result could imply there is an additional, earlier weakening in the early-1700s relating to prior freshwater fluxes as the LIA begins to subside.

The findings presented in this thesis aid the understanding of GS, and perhaps AMOC, states on timescales beyond those covered by instrumental data. They may help to constrain estimates of future AMOC states and the timing of a tipping event. This thesis has reconstructed Bermudan SST variability back to the mid-1400s and found evidence of northward GS path migration in the early 1700s.

7 REFERENCES

Ahn, J., Brook, E.J., Mitchell, L., Rosen, J., McConnell, J.R., Taylor, K., Etheridge, D., Rubino, M., 2012. Atmospheric CO_2 over the last 1000 years: A high-resolution record from the West Antarctic Ice Sheet (WAIS) Divide ice core. Global Biogeochemical Cycles 26, GB2027.

Baker, A., Bradley, C., 2010. Modern stalagmite $\delta^{18}O$: Instrumental calibration and forward modelling. Global and Planetary Change 71, 201-206.

Baker, A., Mariethoz, G., Comas-Bru, L., Hartmann, A., Frisia, S., Borsato, A., Treble, P.C., Asrat, A., 2021. The Properties of Annually Laminated Stalagmites-A Global Synthesis. Reviews of Geophysics 59, e2020RG000722.

Baldini, J.U.L., Lechleitner, F.A., Breitenbach, S.F.M., van Hunen, J., Baldini, L.M., Wynn, P.M., Jamieson, R.A., Ridley, H.E., Baker, A.J., Walczak, I.W., Fohlmeister, J., 2021. Detecting and quantifying palaeoseasonality in stalagmites using geochemical and modelling approaches. Quaternary Science Reviews 254, 106784.

Baldini, L.M., McDermott, F., Baldini, J.U.L., Arias, P., Cueto, M., Fairchild, I.J., Hoffmann, D.L., Mattey, D.P., Müller, W., Nita, D.C., Ontañón, R., García-Moncó, C., Richards, D.A., 2015. Regional temperature, atmospheric circulation, and sea-ice variability within the Younger Dryas Event constrained using a speleothem from northern Iberia. Earth and Planetary Science Letters 419, 101-110.

Beck, J.W., Richards, D.A., Lawrence, R., Silverman, B.W., Smart, P.L., Donahue, D.J., Hererra-Osterheld, S., Burr, G.S., Calsoyas, L., Timothy, A., 2001. Extremely large variations of atmospheric ^{14}C concentration during the last glacial period. Science 292, 2453-2458.

Bhatta, K.P., Mottl, O., Felde, V.A., Flantua, S.G., Birks, H.H., Cao, X., Chen, F., Grytnes, J.A., Seddon, A.W., Birks, H.J.B., 2023. Exploring spatio-temporal patterns of palynological changes in Asia during the Holocene. Frontiers in Ecology and Evolution 11, 1115784.

Belli, R., Borsato, A., Frisia, S., Drysdale, R., Maas, R., Greig, A., 2017. Investigating the hydrological significance of stalagmite geochemistry (Mg, Sr) using Sr isotope and particulate element records across the Late Glacial-to-Holocene transition. Geochimica Et Cosmochimica Acta 199, 247-263.

Bermuda Weather Service, 2018. Climate Data. (available at https://www.weather.bm/climate.asp).

Black, D.E., Abahazi, M.A., Thunell, R.C., Kaplan, A., Tappa, E.J., Peterson, L.C., 2007. An 8-century tropical Atlantic SST record from the Cariaco Basin: Baseline variability, twentieth-century warming, and Atlantic hurricane frequency. Paleoceanography 22, PA4204.

Breitenbach, S.F.M., Rehfeld, K., Goswami, B., Baldini, J.U.L., Ridley, H.E., Kennett, D.J., Prufer, K.M., Aquino, V.V., Asmerom, Y., Polyak, V.J., Cheng, H., Kurths, J., Marwan, N., 2012. COnstructing Proxy Records from Age models (COPRA). Climate of the Past 8, 1765-1779.

Broecker, W.S., 2000. Was a change in thermohaline circulation responsible for the Little Ice Age? Proceedings of the National Academy of Sciences of the United States of America 97, 1339-1342.

Buckley, M.W., Marshall, J., 2016. Observations, inferences, and mechanisms of the Atlantic Meridional Overturning Circulation: A review. Reviews of Geophysics 54, 5-63.

Buhl, D., Immenhauser, A., Smeulders, G., Kabiri, L., Richter, D.K., 2007. Time series δ^{26}Mg analysis in speleothem calcite:: Kinetic versus equilibrium fractionation, comparison with other proxies and implications for palaeoclimate research. Chemical Geology 244, 715-729.

Burton, E.A., Walter, L.M., 1991. The Effects of PCO_2 and Temperature on Magnesium Incorporation in Calcite in Seawater and $MgCl_2$-$CaCl_2$ Solutions. Geochimica Et Cosmochimica Acta 55, 777-785.

Caesar, L., McCarthy, G.D., Thornalley, D.J.R., Cahill, N., Rahmstorf, S., 2021. Current Atlantic Meridional Overturning Circulation weakest in last millennium. Nature Geoscience 14, 118-120.

Caesar, L., Rahmstorf, S., Robinson, A., Feulner, G., Saba, V., 2018. Observed fingerprint of a weakening Atlantic Ocean overturning circulation. Nature 556, 191-196.

Carlson, P.E., Miller, N.R., Banner, J.L., Breecker, D.O., Casteel, R.C., 2018. The potential of near-entrance stalagmites as high-resolution terrestrial paleoclimate proxies: Application of isotope and trace-element geochemistry to seasonally-resolved chronology. Geochimica Et Cosmochimica Acta 235, 55-75.

Chaudhuri, A.H., Gangopadhyay, A., Bisagni, J.J., 2011. Response of the Gulf Stream transport to characteristic high and low phases of the North Atlantic Oscillation. Ocean Modelling 39, 220-232.

Cheng, H., Edwards, R.L., Shen, C.-C., Polyak, V.J., Asmerom, Y., Woodhead, J., Hellstrom, J., Wang, Y., Kong, X., Spötl, C., 2013. Improvements in ^{230}Th dating, ^{230}Th and ^{234}U half-life values, and U–Th isotopic measurements by multi-collector inductively coupled plasma mass spectrometry. Earth and Planetary Science Letters 371, 82-91.

Chester, R., 2009. Marine geochemistry. John Wiley & Sons.

Cisneros, M., Cacho, I., Moreno, A., Stoll, H., Torner, J., Català, A., Edwards, R.L., Cheng, H., Fornós, J.J., 2021. Hydroclimate variability during the last 2700

years based on stalagmite multi-proxy records in the central-western Mediterranean. Quaternary Science Reviews 269, 107137.

Cochrane, D., Orcutt, G.H., 1949. Application of Least Squares Regression to Relationships Containing Autocorrelated Error Terms. Journal of the American Statistical Association 44, 32-61.

Cook, E.R., Kairiukstis, L.A., 2013. Methods of dendrochronology: applications in the environmental sciences. Springer Science & Business Media.

Cook, E.R., Krusic, P.J., Anchukaitis, K.J., Buckley, B.M., Nakatsuka, T., Sano, M., Asia2K, P., 2013. Tree-ring reconstructed summer temperature anomalies for temperate East Asia since 800 CE. Climate Dynamics 41, 2957-2972.

Copernicus Marine Service, 2024. ODYSSEA Global Sea Surface Temperature Gridded Level 4 Daily Multi-Sensor Observations. Copernicus Marine Service. (available at https://doi.org/10.48670/mds-00321).

Cronin, T.M., Hayo, K., Thunell, R.C., Dwyer, G.S., Saenger, C., Willard, D.A., 2010. The Medieval Climate Anomaly and Little Ice Age in Chesapeake Bay and the North Atlantic Ocean. Palaeogeography Palaeoclimatology Palaeoecology 297, 299-310.

Cruz, F.W., Burns, S.J., Jercinovic, M., Karmann, I., Sharp, W.D., Vuille, M., 2007. Evidence of rainfall variations in Southern Brazil from trace element ratios (Mg/Ca and Sr/Ca) in a Late Pleistocene stalagmite. Geochimica Et Cosmochimica Acta 71, 2250-2263.

Dansgaard, W., Clausen, H.B., Gundestrup, N., Hammer, C.U., Johnsen, S.F., Kristinsdottir, P.M., Reeh, N., 1982. A New Greenland Deep Ice Core. Science 218, 1273-1277.

Denniston, R.F., Asmerom, Y., Lachniet, M., Polyak, V.J., Hope, P., An, N., Rodzinyak, K., Humphreys, W.F., 2013. A Last Glacial Maximum through middle Holocene stalagmite record of coastal Western Australia climate. Quaternary Science Reviews 77, 101-112.

Ditlevsen, P., Ditlevsen, S., 2023. Warning of a forthcoming collapse of the Atlantic meridional overturning circulation. Nature Communications 14, 1-12.

Draschba, S., Pätzold, J., Wefer, G., 2000. North Atlantic climate variability since AD 1350 recorded in δ 18 O and skeletal density of Bermuda corals. International Journal of Earth Sciences 88, 733-741.

Drysdale, R., Couchoud, I., Zanchetta, G., Isola, I., Regattieri, E., Hellstrom, J., Govin, A., Tzedakis, P.C., Ireland, T., Corrick, E., Greig, A., Wong, H., Piccini, L., Holden, P., Woodhead, J., 2020. Magnesium in subaqueous speleothems as a potential palaeotemperature proxy. Nature Communications 11, 5027.

Drysdale, R.N., Zanchetta, G., Baneschi, I., Guidi, M., Isola, I., Couchoud, I., Piccini, L., Greig, A., Wong, H., Woodhead, J.D., Regattieri, E., Corrick, E., Paul, B., Spötl, C., Denson, E., Gordon, J., Jaillet, S., Dux, F., Hellstrom, J.C., 2019. Partitioning of Mg, Sr, Ba and U into a subaqueous calcite speleothem. Geochimica Et Cosmochimica Acta 264, 67-91.

Duan, W.H., Wu, S.T., Wang, X.F., Shen, J.H., Xiao, Z.Y., Cui, L.L., Tan, M., 2024. Ma/Ca Ratio in Stalagmites as a Potential Palaeo-Temperature Indicator. Geophysical Research Letters 51, e2024GL108498.

Duesing, W., Kaboth-Bahr, S., Asrat, A., Cohen, A.S., Foerster, V., Lamb, H.F., Schaebitz, F., Trauth, M.H. and Viehberg, F., 2021. Changes in the cyclicity and variability of the eastern African paleoclimate over the last 620 kyrs. Quaternary Science Reviews 273, 107219.

Evans, D., Erez, J., Oron, S., Müller, W., 2015. Mg/Ca-temperature and seawater-test chemistry relationships in the shallow-dwelling large benthic foraminifera Operculina ammonoides. Geochimica et Cosmochimica Acta 148, 325-342.

Fairchild, I.J., Baker, A., 2012. Speleothem science: from process to past environments. John Wiley & Sons.

Fairchild, I.J., Borsato, A., Tooth, A.F., Frisia, S., Hawkesworth, C.J., Huang, Y.M., McDermott, F., Spiro, B., 2000. Controls on trace element (Sr-Mg) compositions of carbonate cave waters: implications for speleothem climatic records. Chemical Geology 166, 255-269.

Fairchild, I.J., Smith, C.L., Baker, A., Fuller, L., Spötl, C., Mattey, D., McDermott, F., Eimp, 2006. Modification and preservation of environmental signals in speleothems. Earth-Science Reviews 75, 105-153.

Fairchild, I.J., Treble, P.C., 2009. Trace elements in speleothems as recorders of environmental change. Quaternary Science Reviews 28, 449-468.

Faraji, M., Borsato, A., Frisia, S., Hellstrom, J.C., Lorrey, A., Hartland, A., Greig, A., Mattey, D.P., 2021. Accurate dating of stalagmites from low seasonal contrast tropical Pacific climate using Sr 2D maps, fabrics and annual hydrological cycles. Scientific Reports 11, 2178.

Fensterer, C., Scholz, D., Hoffmann, D., Spötl, C., Pajón, J.M., Mangini, A., 2012. Cuban stalagmite suggests relationship between Caribbean precipitation and the Atlantic Multidecadal Oscillation during the past 1.3 ka. The Holocene 22, 1405-1412.

Feulner, G., Rahmstorf, S., Levermann, A., Volkwardt, S., 2013. On the Origin of the Surface Air Temperature Difference between the Hemispheres in Earth's Present-Day Climate. Journal of Climate 26, 7136-7150.

Fohlmeister, J., Lechleitner, F.A., 2019. STAlagmite dating by radiocarbon (star): A software tool for reliable and fast age depth modelling. Quaternary Geochronology 51, 120-129.

Galy, A., Bar-Matthews, M., Halicz, L., O'Nions, R.K., 2002. Mg isotopic composition of carbonate: insight from speleothem formation. Earth and Planetary Science Letters 201, 105-115.

Genty, D., Blamart, D., Ghaleb, B., Plagnes, V., Causse, C., Bakalowicz, M., Zouari, K., Chkir, N., Hellstrom, J., Wainer, K., Bourges, F., 2006. Timing and dynamics of the last deglaciation from European and North African $\delta^{13}C$

stalagmite profiles - comparison with Chinese and South Hemisphere stalagmites. Quaternary Science Reviews 25, 2118-2142.

Goodkin, N.F., Hughen, K.A., Curry, W.B., Doney, S.C., Ostermann, D.R., 2008. Sea surface temperature and salinity variability at Bermuda during the end of the Little Ice Age. Paleoceanography 23, PA3203.

Gottschalk, J., Skinner, L.C., Misra, S., Waelbroeck, C., Menviel, L., Timmermann, A., 2015. Abrupt changes in the southern extent of North Atlantic Deep Water during Dansgaard-Oeschger events. Nature Geoscience 8, 950-954.

Hearty, P.J., Vacher, H.L., 1994. Quaternary Stratigraphy of Bermuda - a High-Resolution Pre-Sangamonian Rock Record. Quaternary Science Reviews 13, 685-697.

Hellstrom, J., 2006. U–Th dating of speleothems with high initial ^{230}Th using stratigraphical constraint. Quaternary Geochronology 1, 289-295.

Hodge, E., McDonald, J., Fischer, M., Redwood, D., Hua, Q., Levchenko, V., Drysdale, R., Waring, C., Fink, D., 2011. Using the ^{14}C Bomb Pulse to Date Young Speleothems. Radiocarbon 53, 345-357.

Hoffmann, D.L., Beck, J.W., Richards, D.A., Smart, P.L., Singarayer, J.S., Ketchmark, T., Hawkesworth, C.J., 2010. Towards radiocarbon calibration beyond 28 ka using speleothems from the Bahamas. Earth and Planetary Science Letters 289, 1-10.

Hoffmann, D.L., Prytulak, J., Richards, D.A., Elliott, T., Coath, C.D., Smart, P.L., Scholz, D., 2007. Procedures for accurate U and Th isotope measurements by high precision MC-ICPMS. International Journal of Mass Spectrometry 264, 97-109.

Hofmann, M., Rahmstorf, S., 2009. On the stability of the Atlantic meridional overturning circulation. Proceedings of the National Academy of Sciences of the United States of America 106, 20584-20589.

Huang, H.M., Fairchild, I.J., Borsato, A., Frisia, S., Cassidy, N.J., McDermott, F., Hawkesworth, C.J., 2001. Seasonal variations in Sr, Mg and P in modern speleothems (Grotta di Ernesto, Italy). Chemical Geology 175, 429-448.

Huang, S., Cai, Y., Cheng, H., Xue, G., Cheng, X., He, M., Li, R., Ma, L., Wei, Y., Lu, Y., 2024. An integrated study of constraining the initial ^{230}Th of a stalagmite and its implications. Quaternary Geochronology 80, 101497.

Huang, Y.M., Fairchild, I.J., 2001. Partitioning of Sr^{2+} and Mg^{2+} into calcite under karst-analogue experimental conditions. Geochimica Et Cosmochimica Acta 65, 47-62.

Hurrell, J.W., Kushnir, Y., Ottersen, G., Visbeck, M., 2003. An overview of the North Atlantic oscillation., Geophysical Monograph-American Geophysical Union, pp. 1-36.

Iliffe, T.M., Calderón-Gutiérrez, F., 2021. Bermuda's Walsingham Caves: A Global Hotspot for Anchialine Stygobionts. Diversity 13, 352.

Immenhauser, A., Buhl, D., Richter, D., Niedermayr, A., Riechelmann, D., Dietzel, M., Schulte, U., 2010. Magnesium-isotope fractionation during low-Mg calcite precipitation in a limestone cave - Field study and experiments. Geochimica Et Cosmochimica Acta 74, 4346-4364.

Jamieson, R.A., 2017. Trace element geochemistry of Belizean and Bermudan stalagmites: new tools, proxies and applications., Earth Sciences. Durham University, Durham, United Kingdom. (available at https://etheses.dur.ac.uk/12055/).

Jia, W., Zhang, P.Z., Zhang, L.L., Li, X.H., Gao, T., Wang, H.C., Zhang, H.W., Li, H.Y., Cheng, H., Edwards, R.L., 2022. Highly resolved $\delta^{13}C$ and trace element ratios of precisely dated stalagmite from northwestern China: Hydroclimate reconstruction during the last two millennia. Quaternary Science Reviews 291, 107473.

Joyce, T.M., Kwon, Y.O., Seo, H., Ummenhofer, C.C., 2019. Meridional Gulf Stream Shifts Can Influence Wintertime Variability in the North Atlantic Storm Track and Greenland Blocking. Geophysical Research Letters 46, 1702-1708.

Keigwin, L.D., Pickart, R.S., 1999. Slope water current over the Laurentian Fan on interannual to millennial time scales. Science 286, 520-523.

Kuhnert, H., Pätzold, J., Schnetger, B., Wefer, G., 2002. Sea-surface temperature variability in the 16th century at Bermuda inferred from coral records. Palaeogeography Palaeoclimatology Palaeoecology 179, 159-171.

Lapointe, F., Bradley, R.S., 2021. Little Ice Age abruptly triggered by intrusion of Atlantic waters into the Nordic Seas. Science Advances 7, eabi8230.

Lechleitner, F.A., Fohlmeister, J., McIntyre, C., Baldini, L.M., Jamieson, R.A., Hercman, H., Gasiorowski, M., Pawlak, J., Stefaniak, K., Socha, P., Eglinton, T.I., Baldini, J.U.L., 2016. A novel approach for construction of radiocarbon-based chronologies for speleothems. Quaternary Geochronology 35, 54-66.

Li, X.L., Cui, X.P., He, D., Liao, J., Hu, C.Y., 2018. Evaluation of the Heshang Cave stalagmite calcium isotope composition as a paleohydrologic proxy by comparison with the instrumental precipitation record. Scientific Reports 8, 2615.

Little, C.M., Hu, A.X., Hughes, C.W., McCarthy, G.D., Piecuch, C.G., Ponte, R.M., Thomas, M.D., 2019. The Relationship Between US East Coast Sea Level and the Atlantic Meridional Overturning Circulation: A Review. Journal of Geophysical Research-Oceans 124, 6435-6458.

Longerich, H., Jackson, S., Gunther, D., 1996. Inter-laboratory note. Laser ablation inductively coupled plasma mass spectrometric transient signal data acquisition and analyte concentration calculation. Journal of analytical atomic spectrometry, pp. 899-904.

Lund, D.C., Lynch-Stieglitz, J., Curry, W.B., 2006. Gulf Stream density structure and transport during the past millennium. Nature 444, 601-604.

Luterbacher, J., Xoplaki, E., Dietrich, D., Jones, P.D., Davies, T.D., Portis, D., Gonzalez-Rouco, J.F., von Storch, H., Gyalistras, D., Casty, C., Wanner, H., 2001. Extending North Atlantic Oscillation reconstructions back to 1500. Atmospheric Science Letters 2, 114-124.

Mangini, A., Spötl, C., Verdes, P., 2005. Reconstruction of temperature in the Central Alps during the past 2000 yr from a $\delta^{18}O$ stalagmite record. Earth and Planetary Science Letters 235, 741-751.

Mann, M.E., Zhang, Z.H., Hughes, M.K., Bradley, R.S., Miller, S.K., Rutherford, S., Ni, F.B., 2008. Proxy-based reconstructions of hemispheric and global surface temperature variations over the past two millennia. Proceedings of the National Academy of Sciences of the United States of America 105, 13252-13257.

Marcott, S.A., Clark, P.U., Padman, L., Klinkhammer, G.P., Springer, S.R., Liu, Z.Y., Otto-Bliesner, B.L., Carlson, A.E., Ungerer, A., Padman, J., He, F., Cheng, J., Schmittner, A., 2011. Ice-shelf collapse from subsurface warming as a trigger for Heinrich events. Proceedings of the National Academy of Sciences of the United States of America 108, 13415-13419.

McCarthy, G.D., Joyce, T.M., Josey, S.A., 2018. Gulf Stream Variability in the Context of Quasi-Decadal and Multidecadal Atlantic Climate Variability. Geophysical Research Letters 45, 11257-11264.

Medhaug, I., Langehaug, H.R., Eldevik, T., Furevik, T., Bentsen, M., 2012. Mechanisms for decadal scale variability in a simulated Atlantic meridional overturning circulation. Climate Dynamics 39, 77-93.

Moseley, G.E., Richards, D.A., Smart, P.L., Standish, C.D., Hoffmann, D.L., ten Hove, H., Vinn, O., 2015. Early–middle Holocene relative sea-level oscillation events recorded in a submerged speleothem from the Yucatán Peninsula, Mexico. The Holocene 25, 1511-1521.

Müller, W., Shelley, M., Miller, P., Broude, S., 2009. Initial performance metrics of a new custom-designed ArF excimer LA-ICPMS system coupled to a two-volume laser-ablation cell. Journal of Analytical Atomic Spectrometry 24, 209-214.

Ortega, P., Lehner, F., Swingedouw, D., Masson-Delmotte, V., Raible, C.C., Casado, M., Yiou, P., 2015. A model-tested North Atlantic Oscillation reconstruction for the past millennium. Nature 523, 71-74.

Osman, M.B., Das, S.B., Trusel, L.D., Evans, M.J., Fischer, H., Grieman, M.M., Kipfstuhl, S., McConnell, J.R., Saltzman, E.S., 2019. Industrial-era decline in subarctic Atlantic productivity. Nature 569, 551-555.

Oster, J.L., Weisman, I.E., Sharp, W.D., 2020. Multi-proxy stalagmite records from northern California reveal dynamic patterns of regional hydroclimate over the last glacial cycle. Quaternary Science Reviews 241, 106411.

Palter, J.B., 2015. The Role of the Gulf Stream in European Climate. Annual Review of Marine Science 7, 113-137.

Paton, C., Hellstrom, J., Paul, B., Woodhead, J., Hergt, J., 2011. Iolite: Freeware for the visualisation and processing of mass spectrometric data. Journal of Analytical Atomic Spectrometry 26, 2508-2518.

Peel, M.C., Finlayson, B.L., McMahon, T.A., 2007. Updated world map of the Koppen-Geiger climate classification. Hydrology and Earth System Sciences 11, 1633-1644.

Pinto, J.G., Raible, C.C., 2012. Past and recent changes in the North Atlantic oscillation. Wiley Interdisciplinary Reviews-Climate Change 3, 79-90.

Proctor, C.J., Baker, A., Barnes, W.L., Gilmour, R.A., 2000. A thousand year speleothem proxy record of North Atlantic climate from Scotland. Climate Dynamics 16, 815-820.

Rahmstorf, S., 2002. Ocean circulation and climate during the past 120,000 years. Nature 419, 207-214.

Rahmstorf, S., 2024. Is the Atlantic Overturning Circulation approaching a tipping point? Oceanography.

Rahmstorf, S., Box, J.E., Feulner, G., Mann, M.E., Robinson, A., Rutherford, S., Schaffernicht, E.J., 2015. Exceptional twentieth-century slowdown in Atlantic Ocean overturning circulation. Nature Climate Change 5, 475-480.

Raible, C.C., Pinto, J.G., Ludwig, P., Messmer, M., 2021. A review of past changes in extratropical cyclones in the northern hemisphere and what can be learned for the future. Wiley Interdisciplinary Reviews-Climate Change 12, e680.

Rashid, H., Zhang, Z.W., Piper, D.J.W., Patro, R., Xu, Y.P., 2023. Impact of Medieval Climate Anomaly and Little Ice Age on the Labrador Current flow speed and the AMOC reconstructed by the sediment dynamics and biomarker proxies. Palaeogeography Palaeoclimatology Palaeoecology 620, 111558.

Rayner, N.A., Parker, D.E., Horton, E.B., Folland, C.K., Alexander, L.V., Rowell, D.P., Kent, E.C., Kaplan, A., 2003. Global analyses of sea surface temperature, sea ice, and night marine air temperature since the late nineteenth century. Journal of Geophysical Research-Atmospheres 108, 4407.

Richards, D.A., Dorale, J.A., 2003. Uranium-series chronology and environmental applications of speleothems. Reviews in Mineralogy and Geochemistry 52, 407-460.

Riechelmann, S., Buhl, D., Schröder-Ritzrau, A., Riechelmann, D.F.C., Richter, D.K., Vonhof, H.B., Wassenburg, J.A., Geske, A., Spötl, C., Immenhauser, A., 2012. The magnesium isotope record of cave carbonate archives. Climate of the Past 8, 1849-1867.

Rivera-Collazo, I., Winter, A., Scholz, D., Mangini, A., Miller, T., Kushnir, Y., Black, D., 2015. Human adaptation strategies to abrupt climate change in Puerto Rico ca. 3.5 ka. The Holocene 25, 627-640.

Rouse, J.R.P., 2016. The Provenance and Geochemical Alteration of Bermudan Eolianites. Queen's University, Canada.

Saenger, C., Cohen, A.L., Oppo, D.W., Halley, R.B., Carilli, J.E., 2009. Surface-temperature trends and variability in the low-latitude North Atlantic since 1552. Nature Geoscience 2, 492-495.

Salzer, M.W., Kipfmueller, K.F., 2005. Reconstructed temperature and precipitation on a millennial timescale from tree-rings in the Southern Colorado Plateau, USA. Climatic Change 70, 465-487.

Sanchez-Franks, A., Hameed, S., Wilson, R.E., 2016. The Icelandic Low as a Predictor of the Gulf Stream North Wall Position. Journal of Physical Oceanography 46, 817-826.

Schimpf, D., Kilian, R., Kronz, A., Simon, K., Spötl, C., Wörner, G., Deininger, M., Mangini, A., 2011. The significance of chemical, isotopic, and detrital components in three coeval stalagmites from the superhumid southernmost Andes (53°S) as high-resolution palaeo-climate proxies. Quaternary Science Reviews 30, 443-459.

Schleussner, C.F., Divine, D.V., Donges, J.F., Miettinen, A., Donner, R.V., 2015. Indications for a North Atlantic ocean circulation regime shift at the onset of the Little Ice Age. Climate Dynamics 45, 3623-3633.

Seidov, D., Mishonov, A., Reagan, J., Parsons, R., 2019. Resilience of the Gulf Stream path on decadal and longer timescales. Scientific Reports 9, 11549.

Seip, K.L., Grøn, Ø. and Wang, H., 2019. The North Atlantic Oscillations: Cycle times for the NAO, the AMO and the AMOC. Climate 7(3), 43.

Sinclair, D.J., Banner, J.L., Taylor, F.W., Partin, J., Jenson, J., Mylroie, J., Goddard, E., Quinn, T., Jocson, J., Miklavic, B., 2012. Magnesium and strontium systematics in tropical speleothems from the Western Pacific. Chemical Geology 294, 1-17.

Smolders, E.J., van Westen, R.M., Dijkstra, H.A., 2024. Probability Estimates of a 21st Century AMOC Collapse. arXiv preprint, arXiv:2406.11738.

Spooner, P.T., Thornalley, D.J.R., Oppo, D.W., Fox, A.D., Radionovskaya, S., Rose, N.L., Mallett, R., Cooper, E., Roberts, J.M., 2020. Exceptional 20th Century Ocean Circulation in the Northeast Atlantic. Geophysical Research Letters 47, e2020GL087577.

Stoll, H.M., Müller, W., Prieto, M., 2012. I-STAL, a model for interpretation of Mg/Ca, Sr/Ca and Ba/Ca variations in speleothems and its forward and inverse application on seasonal to millennial scales. Geochemistry, Geophysics, Geosystems 13.

Stommel, H., 1961. Thermohaline Convection with 2 Stable Regimes of Flow. Tellus 13, 224-230.

Swart, P.K., Thorrold, S., Rosenheim, B., Eisenhauer, A., Harrison, C.G.A., Grammer, M., Latkoczy, C., 2002. Intra-annual variation in the stable oxygen and carbon and trace element composition of sclerosponges. Paleoceanography 17, 1045.

Taylor, A.H., Stepens, J.A., 1998. The North Atlantic oscillation and the latitude of the Gulf Stream. Tellus Series a-Dynamic Meteorology and Oceanography 50, 134-142.

Thibodeau, B., Not, C., Hu, J., Schmittner, A., Noone, D., Tabor, C., Zhang, J.X., Liu, Z.Y., 2018. Last Century Warming Over the Canadian Atlantic Shelves Linked to Weak Atlantic Meridional Overturning Circulation. Geophysical Research Letters 45, 12376-12385.

Thornalley, D.J.R., Oppo, D.W., Ortega, P., Robson, J.I., Brierley, C.M., Davis, R., Hall, I.R., Moffa-Sanchez, P., Rose, N.L., Spooner, P.T., Yashayaev, I., Keigwin, L.D., 2018. Anomalously weak Labrador Sea convection and Atlantic overturning during the past 150 years. Nature 556, 227-230.

Trauth, M.H., Foerster, V., Junginger, A., Asrat, A., Lamb, H.F. and Schaebitz, F., 2018. Abrupt or gradual? Change point analysis of the late Pleistocene–Holocene climate record from Chew Bahir, southern Ethiopia. Quaternary Research 90(2), 321-330.

Treble, P., Shelley, J.M.G., Chappell, J., 2003. Comparison of high resolution sub-annual records of trace elements in a modern (1911-1992) speleothem with instrumental climate data from southwest Australia. Earth and Planetary Science Letters 216, 141-153.

Treble, P.C., Fairchild, I.J., Griffiths, A., Baker, A., Meredith, K.T., Wood, A., McGuire, E., 2015. Impacts of cave air ventilation and in-cave prior calcite precipitation on Golgotha Cave dripwater chemistry, southwest Australia. Quaternary Science Reviews 127, 61-72.

Tremaine, D.M., Froelich, P.N., 2013. Speleothem trace element signatures: A hydrologic geochemical study of modern cave dripwaters and farmed calcite. Geochimica Et Cosmochimica Acta 121, 522-545.

Tremaine, D.M., Sinclair, D.J., Stoll, H.M., Lagerström, M., Carvajal, C.P., Sherrell, R.M., 2016. A two-year automated dripwater chemistry study in a remote cave in the tropical south Pacific: Using Cl− as a conservative tracer for seasalt contribution of major cations. Geochimica et Cosmochimica Acta 184, 289-310.

Trouet, V., Esper, J., Graham, N.E., Baker, A., Scourse, J.D., Frank, D.C., 2009. Persistent Positive North Atlantic Oscillation Mode Dominated the Medieval Climate Anomaly. Science 324, 78-80.

Trouet, V., Scourse, J.D., Raible, C.C., 2012. North Atlantic storminess and Atlantic Meridional Overturning Circulation during the last Millennium: Reconciling contradictory proxy records of NAO variability. Global and Planetary Change 84-85, 48-55.

Vacher, H., Hearty, P., Rowe, M., Curran, H., White, B., 1995. Stratigraphy of Bermuda: nomenclature, concepts, and status of multiple systems of classification. Special Papers-Geological Society of America, 271-294.

van Calsteren, P., Thomas, L., 2006. Uranium-series dating applications in natural environmental science. Earth-Science Reviews 75, 155-175.

van Westen, R.M., Kliphuis, M., Dijkstra, H.A., 2024. Physics-based early warning signal shows that AMOC is on tipping course. Science Advances 10, eadk1189.

Vermeesch, P., 2018. IsoplotR: A free and open toolbox for geochronology. Geoscience Frontiers 9, 1479-1493.

Waite, A.J., Klavans, J.M., Clement, A.C., Murphy, L.N., Liebetrau, V., Eisenhauer, A., Weger, R.J., Swart, P.K., 2020. Observational and Model Evidence for an Important Role for Volcanic Forcing Driving Atlantic Multidecadal Variability Over the Last 600 Years. Geophysical Research Letters 47, e2020GL089428.

Walczak, I., 2016. Holocene climate variability revealed using geochemistry and Computed Tomography scanning of stalagmites from the North Atlantic Basin., Earth Sciences. Durham University, Durham, United Kingdom. (available at https://etheses.dur.ac.uk/12140/).

Wanner, H., Pfister, C., Neukom, R., 2022. The variable European Little Ice Age. Quaternary Science Reviews 287, 107531.

Warken, S.F., Vieten, R., Winter, A., Spötl, C., Miller, T.E., Jochum, K.P., Schröder-Ritzrau, A., Mangini, A., Scholz, D., 2020. Persistent link between Caribbean precipitation and Atlantic Ocean circulation during the Last Glacial revealed by a speleothem record from Puerto Rico. Paleoceanography and Paleoclimatology 35, e2020PA003944.

Wassenburg, J.A., Riechelmann, S., Schröder-Ritzrau, A., Riechelmann, D.F.C., Richter, D.K., Immenhauser, A., Terente, M., Constantin, S., Hachenberg, A., Hansen, M., Scholz, D., 2020. Calcite Mg and Sr partition coefficients in cave environments: Implications for interpreting prior calcite precipitation in speleothems. Geochimica Et Cosmochimica Acta 269, 581-596.

Wei, G.J., McCulloch, M.T., Mortimer, G., Deng, W.F., Xie, L.H., 2009. Evidence for ocean acidification in the Great Barrier Reef of Australia. Geochimica Et Cosmochimica Acta 73, 2332-2346.

Whitney, N.M., Wanamaker, A.D., Ummenhofer, C.C., Johnson, B.J., Cresswell-Clay, N., Kreutz, K.J., 2022. Rapid 20th century warming reverses 900-year cooling in the Gulf of Maine. Communications Earth & Environment 3, 179.

Wong, C.I., Banner, J.L., Musgrove, M., 2011. Seasonal dripwater Mg/Ca and Sr/Ca variations driven by cave ventilation: Implications for and modeling of speleothem paleoclimate records. Geochimica Et Cosmochimica Acta 75, 3514-3529.

Wortham, B.E., Banner, J.L., James, E.W., Edwards, R.L., Loewy, S., 2022. Application of cave monitoring to constrain the value and source of detrital 230Th/232Th in speleothem calcite: Implications for U-series geochronology of speleothems. Palaeogeography, Palaeoclimatology, Palaeoecology 596, 110978.

Wynn, P.M., Fairchild, I.J., Baker, A., Baldini, J.U.L., McDermott, F., 2008. Isotopic archives of sulphate in speleothems. Geochimica Et Cosmochimica Acta 72, 2465-2477.

Yan, H., Sun, L.G., Wang, Y.H., Huang, W., Qiu, S.C., Yang, C.Y., 2011. A record of the Southern Oscillation Index for the past 2,000 years from precipitation proxies. Nature Geoscience 4, 611-614.

Zhang, W.Z., Chai, F., Xue, H.J., Oey, L.Y., 2020. Remote sensing linear trends of the Gulf Stream from 1993 to 2016. Ocean Dynamics 70, 701-712.

Zhao, K., Wulder, M.A., Hu, T., Bright, R., Wu, Q., Qin, H., Li, Y., Toman, E., Mallick, B., Zhang, X. and Brown, M., 2019. Detecting change-point, trend, and seasonality in satellite time series data to track abrupt changes and nonlinear dynamics: A Bayesian ensemble algorithm. Remote sensing of Environment 232, 111181.

Zielinski, G.A., 2000. Use of paleo-records in determining variability within the volcanism-climate system. Quaternary Science Reviews 19, 417-438.

8 APPENDICES

8.1 APPENDIX 1: U-TH DATA

U-series chronological data from Walczak (2016) and Jamieson (2017). Decay constants (Cheng et al., 2013): 9.1705×10^{-6} yr^{-1} for ^{230}Th, 2.8221×10^{-6} yr^{-1} for ^{234}U. Italics indicate replicate analysis on sub-samples. Two standard error uncertainties are arbitrarily selected to be 50%. Table is split up from that in the manuscript due to page constraints but uses the *Sample Name* column as an index.

Sample Name	Lab Code	Depth mm	^{238}U ng/g	Uncertainty ± 2se
BER-SWI-UTh-1	STAiG-UTh-dcn-562	8	94.5	0.3
BER-SWI-UTh-2	BIG-UTh-N-435	15	84.6	0.2
BER-SWI-UTh-3	STAiG-UTh-dcn-561	26	97.9	0.3
BER-SWI-UTh-4	BIG-UTh-N-437	35	98.2	0.3
BER-SWI-UTh-5	STAiG-UTh-dcn-560	47	118.5	0.4
BER-SWI-UTh-6	BIG-UTh-N-439	57.5	135.5	0.3
BER-SWI-UTh-7	STAiG-UTh-dcn-558	67.5	85.9	0.3
BER-SWI-UTh-8	BIG-UTh-N-441	80	110.6	0.3
BER-SWI-UTh-9	STAiG-UTh-dcn-557	96	85.7	0.3
BER-SWI-UTh-10	BIG-UTh-N-451	106	96.8	1.9
BER-SWI-UTh-11	STAiG-UTh-dcn-556	128	86.2	0.3
BER-SWI-UTh-12	BIG-UTh-N-453	156	95.3	1.7
BER-SWI-UTh-13(1)	*STAiG-UTh-dcn-541*		*95.5*	*2.2*
BER-SWI-UTh-13(2)	*STAiG-UTh-dcn-542*		*99.0*	*2.7*
BER-SWI-UTh-13(3)	*STAiG-UTh-dcn-543*		*95.2*	*2.0*
BER-SWI-UTh-13 (mean)		165		
BER-SWI-UTh-14	BIG-UTh-N-455	174	298.6	1.8
BER-SWI-UTh-15(1)	*STAiG-UTh-dcn-538*		*83.7*	*0.2*
BER-SWI-UTh-15(2)	*STAiG-UTh-dcn-539*		*84.1*	*0.3*
BER-SWI-UTh-15(3)	*STAiG-UTh-dcn-540*		*84.1*	*0.3*
BER-SWI-UTh-15 (mean)		179		
BER-SWI-UTh-16	BIG-UTh-N-457	190	362.4	2.1

Sample Name	^{232}Th ng/g	Uncertainty ± 2se	[^{230}Th/^{232}Th] atomic ratio (x10^6)	Uncertainty ± 2se
BER-SWI-UTh-1	0.1907	0.0042	29	0.6
BER-SWI-UTh-2	0.0325	0.0007	82	3.5
BER-SWI-UTh-3	0.0256	0.0006	136	4.0
BER-SWI-UTh-4	0.0552	0.0011	79	3.2
BER-SWI-UTh-5	0.0546	0.0013	197	4.0
BER-SWI-UTh-6	0.0341	0.0007	215	3.9
BER-SWI-UTh-7	0.0283	0.0008	180	4.8
BER-SWI-UTh-8	0.0219	0.0005	333	10.4
BER-SWI-UTh-9	0.0138	0.0006	455	10.4
BER-SWI-UTh-10	0.0171	0.0005	404	10.6
BER-SWI-UTh-11	0.0148	0.0004	462	11.5
BER-SWI-UTh-12	0.0452	0.0013	176	4.7
BER-SWI-UTh-13(1)	*0.0115*	*0.0007*	*691*	*29.9*
BER-SWI-UTh-13(2)	*0.0352*	*0.0017*	*234*	*10.4*
BER-SWI-UTh-13(3)	*0.0127*	*0.0006*	*642*	*24.4*
BER-SWI-UTh-13(mean)				
BER-SWI-UTh-14	0.0635	0.0014	408	8.4
BER-SWI-UTh-15(1)	*0.0122*	*0.0004*	*593*	*21.5*
BER-SWI-UTh-15(2)	*0.0074*	*0.0005*	*997*	*48.9*
BER-SWI-UTh-15(3)	*0.0136*	*0.0005*	*556*	*25.2*
BER-SWI-UTh-15 (mean)				
BER-SWI-UTh-16	0.3551	0.0073	131	2.5

Sample Name	(^{230}Th/^{232}Th) activity ratio	Uncertainty ± 2se	(^{232}Th/^{238}U) activity ratio	Uncertainty ± 2se
BER-SWI-UTh-1	5.3	0.1	0.000660	0.000015
BER-SWI-UTh-2	15.1	0.6	0.000126	0.000003
BER-SWI-UTh-3	25.2	0.7	0.000085	0.000002
BER-SWI-UTh-4	14.6	0.6	0.000184	0.000004
BER-SWI-UTh-5	36.4	0.7	0.000151	0.000004
BER-SWI-UTh-6	39.9	0.7	0.000082	0.000002
BER-SWI-UTh-7	33.3	0.9	0.000108	0.000003
BER-SWI-UTh-8	61.7	1.9	0.000065	0.000001
BER-SWI-UTh-9	84.1	1.9	0.000053	0.000002
BER-SWI-UTh-10	74.7	2.0	0.000058	0.000001
BER-SWI-UTh-11	85.5	2.1	0.000056	0.000002
BER-SWI-UTh-12	32.6	0.9	0.000155	0.000004
BER-SWI-UTh-13(1)	*127.9*	*5.5*	*0.000039*	*0.000002*
BER-SWI-UTh-13(2)	*43.3*	*1.9*	*0.000116*	*0.000004*
BER-SWI-UTh-13(3)	*118.8*	*4.5*	*0.000044*	*0.000002*
BER-SWI-UTh-13(mean)			0.000050	0.000003
BER-SWI-UTh-14	75.6	1.6	0.000070	0.000001
BER-SWI-UTh-15(1)	*109.8*	*4.0*	*0.000048*	*0.000002*
BER-SWI-UTh-15(2)	*184.5*	*9.1*	*0.000029*	*0.000002*
BER-SWI-UTh-15(3)	*103.0*	*4.7*	*0.000053*	*0.000002*
BER-SWI-UTh-15 (mean)			0.000043	0.000002
BER-SWI-UTh-16	24.2	0.5	0.000321	0.000006

Sample Name	($^{234}U/^{238}U$) activity ratio	Uncertainty ± 2se	($^{230}Th/^{238}U$) activity ratio	Uncertainty ± 2se
BER-SWI-UTh-1	1.0604	0.0019	0.00352	0.00021
BER-SWI-UTh-2	1.0578	0.0016	0.00190	0.00022
BER-SWI-UTh-3	1.0566	0.0018	0.00215	0.00018
BER-SWI-UTh-4	1.0519	0.0018	0.00269	0.00036
BER-SWI-UTh-5	1.0542	0.0018	0.00549	0.00024
BER-SWI-UTh-6	1.0538	0.0017	0.00329	0.00023
BER-SWI-UTh-7	1.0548	0.0019	0.00359	0.00024
BER-SWI-UTh-8	1.0606	0.0021	0.00400	0.00031
BER-SWI-UTh-9	1.0607	0.0018	0.00444	0.00027
BER-SWI-UTh-10	1.0608	0.0018	0.00432	0.00032
BER-SWI-UTh-11	1.0579	0.0023	0.00481	0.00030
BER-SWI-UTh-12	1.0619	0.0016	0.00507	0.00032
BER-SWI-UTh-13(1)	*1.0514*	*0.0021*	*0.00502*	*0.00054*
BER-SWI-UTh-13(2)	*1.0500*	*0.0023*	*0.00504*	*0.00060*
BER-SWI-UTh-13(3)	*1.0536*	*0.0024*	*0.00518*	*0.00054*
BER-SWI-UTh-13(mean)	1.0516	0.0026	0.00508	0.00063
BER-SWI-UTh-14	1.0573	0.0018	0.00526	0.00014
BER-SWI-UTh-15(1)	*1.0475*	*0.0020*	*0.00522*	*0.00051*
BER-SWI-UTh-15(2)	*1.0457*	*0.0022*	*0.00531*	*0.00081*
BER-SWI-UTh-15(3)	*1.0432*	*0.0021*	*0.00545*	*0.00072*
BER-SWI-UTh-15 (mean)	1.0455	0.0024	0.00530	0.00073
BER-SWI-UTh-16	1.0566	0.0017	0.00775	0.00015

Sample Name	Age: $^{238}U/^{232}Th$ = 0.8 ± 0.4 ka	Uncertainty ± 2se	Age: $^{238}U/^{232}Th$ = 5 ± 2.5 ka	Uncertainty ± 2se
BER-SWI-UTh-1	0.308	0.022	0.023	0.272
BER-SWI-UTh-2	0.186	0.023	0.131	0.057
BER-SWI-UTh-3	0.215	0.019	0.178	0.040
BER-SWI-UTh-4	0.264	0.037	0.184	0.085
BER-SWI-UTh-5	0.557	0.025	0.491	0.067
BER-SWI-UTh-6	0.334	0.024	0.299	0.042
BER-SWI-UTh-7	0.363	0.025	0.316	0.051
BER-SWI-UTh-8	0.407	0.032	0.379	0.042
BER-SWI-UTh-9	0.453	0.028	0.430	0.035
BER-SWI-UTh-10	0.440	0.033	0.415	0.041
BER-SWI-UTh-11	0.492	0.031	0.468	0.039
BER-SWI-UTh-12	0.509	0.033	0.442	0.072
BER-SWI-UTh-13(1)	*0.519*	*0.055*	*0.502*	*0.059*
BER-SWI-UTh-13(2)	*0.515*	*0.062*	*0.464*	*0.085*
BER-SWI-UTh-13(3)	*0.534*	*0.055*	*0.515*	*0.059*
BER-SWI-UTh-13(mean)	0.524	0.065	0.502	0.069
BER-SWI-UTh-14	0.538	0.055	0.508	0.038
BER-SWI-UTh-15(1)	*0.541*	*0.052*	*0.520*	*0.058*
BER-SWI-UTh-15(2)	*0.553*	*0.083*	*0.540*	*0.085*
BER-SWI-UTh-15(3)	*0.567*	*0.074*	*0.544*	*0.079*
BER-SWI-UTh-15 (mean)	0.551	0.075	0.532	0.078
BER-SWI-UTh-16	0.776	0.016	0.637	0.134

8.2 APPENDIX 2: RADIOCARBON DATA

Radiocarbon chronological data from Walczak (2016) and Jamieson (2017). DCF correction is applied in the 'average' radiocarbon chronological model.

Sample ID	Depth mm	$F^{14}C$ pMC	Error abs.	^{14}C Age year BP	Error years
SWI-14C-01	0	1.0491	0.0032	-385	24
SWI-14C-02	3	1.0048	0.0031	-38	25
SWI-14C-03	7.5	0.9598	0.0030	330	25
SWI-14C-04	12.5	0.9521	0.0028	395	24
SWI-14C-05	17.5	0.9579	0.0030	345	25
SWI-14C-06	22.5	0.9584	0.0029	341	24
SWI-14C-07	27.5	0.9569	0.0029	354	25
SWI-14C-08	32.5	0.9466	0.0028	441	24
SWI-14C-09	37.5	0.9466	0.0029	441	25
SWI-14C-10	42.5	0.9448	0.0028	456	24
SWI-14C-11	47.5	0.9466	0.0029	441	25
SWI-14C-13	57.5	0.9401	0.0030	496	26
SWI-14C-15	67.5	0.9300	0.0029	583	25
SWI-14C-17	77.5	0.9250	0.0029	627	25
SWI-14C-19	87.5	0.9171	0.0029	695	25
SWI-14C-21	97.5	0.9193	0.0029	676	25
SWI-14C-23	107.5	0.9147	0.0029	716	25
SWI-14C-25	117.5	0.9186	0.0029	682	25
SWI-14C-27	127.5	0.9183	0.0028	685	24
SWI-14C-29	137.5	0.9194	0.0028	675	24
SWI-14C-31	147.5	0.9133	0.0027	728	24
SWI-14C-33	157.5	0.9113	0.0028	746	25
SWI-14C-35	167.5	0.9060	0.0027	793	24
SWI-14C-37	177.5	0.9103	0.0028	755	25
SWI-14C-39	192.5	0.9024	0.0028	825	25

8.3 APPENDIX 3: SST RECORD

The annual stalagmite-derived SST record. The upper and lower bounds represent the 95% confidence interval of the regression described in Section 4.5.

Year CE	SST °C	Lower °C	Upper °C
2012	24.00	23.81	24.19
2011	24.04	23.85	24.24
2010	24.03	23.83	24.22
2009	23.96	23.77	24.14
2008	24.07	23.87	24.27
2007	24.01	23.81	24.20
2006	24.05	23.85	24.25
2005	23.99	23.80	24.18
2004	23.80	23.63	23.97
2003	23.80	23.63	23.97
2002	23.87	23.70	24.05
2001	23.82	23.65	23.99
2000	23.74	23.58	23.91
1999	23.76	23.59	23.92
1998	23.80	23.63	23.97
1997	23.76	23.60	23.93
1996	23.77	23.60	23.93
1995	23.71	23.55	23.87

Year CE	SST °C	Lower °C	Upper °C
1994	23.80	23.63	23.97
1993	23.58	23.43	23.72
1992	23.56	23.41	23.70
1991	23.60	23.45	23.75
1990	23.51	23.38	23.65
1989	23.31	23.19	23.43
1988	23.75	23.59	23.91
1987	23.67	23.51	23.83
1986	23.64	23.49	23.79
1985	23.60	23.46	23.75
1984	23.52	23.38	23.66
1983	22.89	22.80	22.98
1982	23.29	23.17	23.41
1981	23.01	22.92	23.11
1980	23.32	23.20	23.44
1979	23.46	23.33	23.60
1978	22.77	22.69	22.86
1977	23.56	23.41	23.70

Year CE	SST °C	Lower °C	Upper °C
1976	23.65	23.50	23.81
1975	23.63	23.48	23.79
1974	23.45	23.32	23.59
1973	23.54	23.40	23.68
1972	23.45	23.32	23.58
1971	23.63	23.48	23.78
1970	23.33	23.21	23.46
1969	23.20	23.09	23.31
1968	23.38	23.25	23.50
1967	23.33	23.21	23.45
1966	22.88	22.79	22.97
1965	23.18	23.07	23.29
1964	23.55	23.41	23.69
1963	22.77	22.69	22.86
1962	22.59	22.51	22.67
1961	22.96	22.86	23.05
1960	23.41	23.29	23.54
1959	23.16	23.05	23.26
1958	23.23	23.11	23.34
1957	23.49	23.35	23.62
1956	22.98	22.89	23.08

Year CE	SST °C	Lower °C	Upper °C
1955	23.45	23.32	23.58
1954	22.88	22.79	22.96
1953	23.01	22.92	23.11
1952	23.07	22.97	23.17
1951	23.11	23.01	23.21
1950	23.86	23.69	24.04
1949	23.98	23.79	24.17
1948	23.58	23.43	23.73
1947	23.25	23.14	23.37
1946	22.27	22.18	22.37
1945	22.29	22.20	22.38
1944	22.68	22.60	22.76
1943	22.50	22.41	22.58
1942	22.97	22.88	23.06
1941	23.63	23.48	23.78
1940	23.32	23.20	23.44
1939	23.19	23.08	23.30
1938	23.29	23.17	23.41
1937	23.71	23.55	23.87
1936	23.67	23.51	23.82
1935	23.58	23.43	23.72

Year CE	SST °C	Lower °C	Upper °C
1934	23.25	23.14	23.37
1933	23.09	22.99	23.19
1932	22.93	22.84	23.02
1931	22.66	22.58	22.74
1930	22.40	22.32	22.49
1929	22.72	22.64	22.81
1928	23.21	23.10	23.32
1927	22.73	22.65	22.81
1926	22.57	22.49	22.65
1925	22.80	22.71	22.88
1924	22.87	22.79	22.96
1923	22.60	22.51	22.68
1922	22.70	22.62	22.79
1921	22.59	22.50	22.67
1920	23.20	23.09	23.31
1919	22.89	22.81	22.98
1918	22.74	22.65	22.82
1917	22.66	22.57	22.74
1916	22.72	22.63	22.80
1915	22.74	22.66	22.82
1914	22.74	22.66	22.83

Year CE	SST °C	Lower °C	Upper °C
1913	22.24	22.15	22.34
1912	22.41	22.32	22.50
1911	22.89	22.80	22.98
1910	22.82	22.74	22.91
1909	22.93	22.83	23.02
1908	22.90	22.81	22.99
1907	22.75	22.67	22.84
1906	23.41	23.28	23.54
1905	23.14	23.04	23.25
1904	22.58	22.50	22.66
1903	22.81	22.72	22.89
1902	23.34	23.21	23.46
1901	23.19	23.08	23.30
1900	23.29	23.17	23.41
1899	23.71	23.55	23.87
1898	23.56	23.42	23.70
1897	23.25	23.13	23.36
1896	23.64	23.49	23.79
1895	23.44	23.31	23.57
1894	23.05	22.95	23.14
1893	23.28	23.16	23.40

Year CE	SST °C	Lower °C	Upper °C
1892	23.34	23.22	23.46
1891	23.10	23.00	23.21
1890	23.29	23.18	23.41
1889	23.39	23.26	23.52
1888	23.51	23.38	23.65
1887	22.78	22.70	22.87
1886	23.29	23.17	23.40
1885	23.02	22.92	23.11
1884	22.89	22.80	22.98
1883	23.02	22.92	23.11
1882	22.69	22.61	22.77
1881	22.86	22.77	22.95
1880	22.20	22.10	22.29
1879	23.07	22.97	23.16
1878	22.68	22.60	22.77
1877	22.62	22.54	22.71
1876	22.75	22.67	22.83
1875	22.26	22.17	22.35
1874	21.93	21.81	22.05
1873	22.03	21.92	22.14
1872	21.57	21.41	21.72

Year CE	SST °C	Lower °C	Upper °C
1871	21.60	21.45	21.76
1870	21.73	21.59	21.87
1869	22.23	22.14	22.33
1868	21.85	21.72	21.97
1867	21.62	21.47	21.77
1866	21.63	21.49	21.78
1865	21.34	21.16	21.52
1864	21.33	21.15	21.51
1863	21.87	21.75	22.00
1862	21.69	21.55	21.83
1861	21.95	21.83	22.06
1860	22.26	22.17	22.35
1859	21.79	21.66	21.93
1858	22.24	22.14	22.33
1857	22.57	22.49	22.66
1856	22.66	22.58	22.74
1855	22.12	22.01	22.22
1854	21.72	21.58	21.85
1853	21.59	21.44	21.74
1852	21.60	21.44	21.75
1851	20.87	20.64	21.10

Year CE	SST °C	Lower °C	Upper °C
1850	21.23	21.03	21.42
1849	21.39	21.22	21.57
1848	21.39	21.22	21.56
1847	21.15	20.95	21.36
1846	21.58	21.43	21.74
1845	22.70	22.62	22.79
1844	22.43	22.34	22.51
1843	21.44	21.27	21.61
1842	21.78	21.65	21.92
1841	21.75	21.61	21.88
1840	21.65	21.51	21.80
1839	21.19	21.00	21.39
1838	21.66	21.51	21.80
1837	22.26	22.17	22.35
1836	21.34	21.16	21.52
1835	21.33	21.15	21.51
1834	21.38	21.21	21.56
1833	22.88	22.79	22.97
1832	21.56	21.41	21.72
1831	21.87	21.74	21.99
1830	22.51	22.43	22.59

Year CE	SST °C	Lower °C	Upper °C
1829	22.12	22.02	22.22
1828	21.91	21.79	22.03
1827	21.58	21.42	21.73
1826	21.67	21.52	21.81
1825	21.83	21.71	21.96
1824	22.57	22.49	22.65
1823	22.35	22.26	22.44
1822	22.05	21.95	22.16
1821	22.29	22.20	22.39
1820	22.46	22.38	22.55
1819	22.32	22.23	22.41
1818	21.70	21.56	21.84
1817	22.40	22.31	22.48
1816	22.05	21.95	22.16
1815	21.44	21.27	21.61
1814	22.67	22.59	22.75
1813	22.64	22.56	22.72
1812	22.16	22.06	22.26
1811	21.74	21.61	21.88
1810	22.82	22.74	22.91
1809	22.79	22.71	22.88

Year CE	SST °C	Lower °C	Upper °C
1808	22.75	22.67	22.84
1807	22.60	22.51	22.68
1806	22.34	22.25	22.43
1805	22.64	22.56	22.72
1804	23.25	23.14	23.37
1803	22.44	22.35	22.52
1802	22.45	22.36	22.53
1801	22.40	22.32	22.49
1800	22.82	22.73	22.90
1799	22.92	22.83	23.01
1798	22.54	22.46	22.62
1797	22.79	22.70	22.87
1796	23.13	23.02	23.23
1795	23.17	23.06	23.27
1794	23.20	23.09	23.31
1793	22.96	22.87	23.05
1792	22.70	22.62	22.78
1791	22.34	22.26	22.43
1790	23.26	23.15	23.38
1789	23.09	22.98	23.19
1788	23.10	22.99	23.20

Year CE	SST °C	Lower °C	Upper °C
1787	22.88	22.79	22.97
1786	22.97	22.87	23.06
1785	23.16	23.06	23.27
1784	23.03	22.93	23.13
1783	22.83	22.75	22.92
1782	23.15	23.05	23.26
1781	22.87	22.78	22.96
1780	22.78	22.69	22.86
1779	22.94	22.85	23.03
1778	23.13	23.02	23.23
1777	22.82	22.74	22.91
1776	23.08	22.98	23.18
1775	23.13	23.03	23.24
1774	22.66	22.58	22.74
1773	22.87	22.79	22.96
1772	23.17	23.07	23.28
1771	23.05	22.95	23.15
1770	22.80	22.71	22.88
1769	23.08	22.98	23.18
1768	23.34	23.22	23.46
1767	23.19	23.08	23.30

Year CE	SST °C	Lower °C	Upper °C
1766	23.37	23.24	23.49
1765	23.41	23.28	23.54
1764	23.37	23.25	23.50
1763	23.24	23.13	23.35
1762	23.49	23.36	23.63
1761	23.42	23.29	23.55
1760	23.40	23.27	23.53
1759	23.58	23.43	23.72
1758	23.56	23.41	23.70
1757	23.59	23.44	23.73
1756	23.29	23.17	23.40
1755	23.14	23.04	23.25
1754	22.71	22.63	22.79
1753	22.77	22.69	22.86
1752	22.90	22.81	22.99
1751	22.99	22.90	23.09
1750	23.02	22.92	23.12
1749	23.05	22.95	23.15
1748	22.42	22.34	22.51
1747	22.93	22.84	23.02
1746	23.70	23.54	23.86

Year CE	SST °C	Lower °C	Upper °C
1745	23.88	23.70	24.06
1744	23.79	23.63	23.96
1743	23.70	23.54	23.86
1742	23.90	23.72	24.08
1741	23.57	23.43	23.72
1740	23.60	23.45	23.75
1739	23.97	23.79	24.16
1738	24.00	23.81	24.20
1737	23.90	23.72	24.09
1736	23.45	23.32	23.58
1735	23.55	23.41	23.69
1734	23.43	23.29	23.56
1733	23.24	23.13	23.35
1732	23.86	23.68	24.04
1731	23.76	23.60	23.93
1730	23.66	23.51	23.82
1729	23.42	23.29	23.54
1728	23.35	23.23	23.47
1727	23.15	23.04	23.26
1726	23.29	23.17	23.41
1725	23.17	23.07	23.28

Year CE	SST °C	Lower °C	Upper °C
1724	23.20	23.09	23.31
1723	23.11	23.01	23.22
1722	23.26	23.14	23.37
1721	23.01	22.92	23.11
1720	23.10	23.00	23.20
1719	23.34	23.22	23.46
1718	23.24	23.12	23.35
1717	23.89	23.71	24.07
1716	23.82	23.64	23.99
1715	23.93	23.75	24.12
1714	24.01	23.82	24.20
1713	23.62	23.47	23.77
1712	24.32	24.09	24.55
1711	24.38	24.15	24.62
1710	24.36	24.13	24.60
1709	24.03	23.83	24.22
1708	24.17	23.96	24.38
1707	23.89	23.71	24.07
1706	23.79	23.62	23.96
1705	23.96	23.77	24.14
1704	23.87	23.69	24.05

Year CE	SST °C	Lower °C	Upper °C
1703	23.56	23.42	23.71
1702	23.94	23.75	24.12
1701	24.18	23.97	24.39
1700	23.99	23.80	24.18
1699	23.78	23.61	23.95
1698	23.84	23.67	24.02
1697	23.63	23.48	23.78
1696	23.75	23.58	23.91
1695	23.88	23.70	24.06
1694	23.98	23.79	24.17
1693	24.04	23.84	24.23
1692	23.87	23.69	24.05
1691	23.63	23.48	23.79
1690	23.77	23.60	23.93
1689	24.22	24.00	24.44
1688	24.27	24.04	24.49
1687	24.28	24.06	24.51
1686	24.21	23.99	24.42
1685	24.16	23.95	24.37
1684	24.06	23.86	24.26
1683	23.70	23.54	23.86

Year CE	SST °C	Lower °C	Upper °C
1682	23.82	23.65	23.99
1681	23.86	23.68	24.04
1680	23.69	23.53	23.85
1679	23.71	23.55	23.87
1678	24.00	23.81	24.19
1677	24.10	23.89	24.30
1676	24.05	23.85	24.25
1675	24.19	23.98	24.41
1674	24.15	23.94	24.36
1673	24.01	23.82	24.21
1672	23.85	23.67	24.02
1671	23.96	23.78	24.15
1670	23.67	23.51	23.82
1669	24.32	24.09	24.55
1668	24.18	23.97	24.40
1667	23.92	23.73	24.10
1666	23.72	23.56	23.88
1665	23.63	23.48	23.78
1664	23.99	23.79	24.18
1663	23.70	23.54	23.86
1662	24.03	23.83	24.22

Year CE	SST °C	Lower °C	Upper °C
1661	23.75	23.58	23.91
1660	23.80	23.63	23.97
1659	23.67	23.51	23.82
1658	23.66	23.51	23.82
1657	23.62	23.47	23.77
1656	23.62	23.47	23.77
1655	23.64	23.49	23.79
1654	23.90	23.72	24.08
1653	23.84	23.67	24.01
1652	23.92	23.74	24.11
1651	23.94	23.75	24.12
1650	23.66	23.50	23.81
1649	23.63	23.48	23.78
1648	23.61	23.46	23.76
1647	24.08	23.88	24.28
1646	23.49	23.35	23.63
1645	23.45	23.32	23.59
1644	23.92	23.73	24.10
1643	24.04	23.84	24.23
1642	23.94	23.75	24.13
1641	23.65	23.50	23.81

Year CE	SST °C	Lower °C	Upper °C
1640	24.47	24.22	24.72
1639	24.16	23.95	24.37
1638	23.91	23.73	24.10
1637	23.85	23.68	24.03
1636	24.07	23.87	24.26
1635	24.10	23.90	24.31
1634	23.80	23.63	23.97
1633	23.72	23.56	23.88
1632	24.23	24.01	24.45
1631	23.89	23.71	24.07
1630	24.13	23.93	24.34
1629	24.07	23.87	24.27
1628	23.87	23.69	24.04
1627	23.75	23.58	23.91
1626	24.13	23.92	24.33
1625	24.27	24.04	24.49
1624	24.06	23.86	24.26
1623	24.14	23.93	24.35
1622	24.27	24.04	24.49
1621	24.08	23.88	24.28
1620	24.00	23.81	24.19

Year CE	SST °C	Lower °C	Upper °C
1619	24.27	24.05	24.50
1618	24.19	23.97	24.40
1617	24.02	23.82	24.21
1616	23.81	23.64	23.98
1615	23.78	23.61	23.95
1614	23.86	23.68	24.03
1613	23.92	23.73	24.10
1612	23.98	23.79	24.16
1611	24.27	24.05	24.49
1610	24.24	24.02	24.46
1609	23.74	23.58	23.91
1608	23.55	23.41	23.70
1607	23.70	23.54	23.85
1606	23.81	23.64	23.98
1605	23.65	23.49	23.80
1604	24.30	24.07	24.52
1603	23.98	23.79	24.17
1602	23.80	23.63	23.97
1601	23.96	23.77	24.15
1600	23.72	23.56	23.88
1599	23.73	23.57	23.89

Year CE	SST °C	Lower °C	Upper °C
1598	23.92	23.74	24.11
1597	23.89	23.71	24.07
1596	23.62	23.47	23.77
1595	23.70	23.54	23.86
1594	23.84	23.67	24.02
1593	23.77	23.60	23.94
1592	23.76	23.60	23.93
1591	23.73	23.57	23.89
1590	23.60	23.45	23.74
1589	24.04	23.84	24.24
1588	24.05	23.85	24.24
1587	24.03	23.83	24.22
1586	24.03	23.84	24.23
1585	23.82	23.65	23.99
1584	23.87	23.70	24.05
1583	23.82	23.65	23.99
1582	24.02	23.83	24.22
1581	24.04	23.84	24.23
1580	23.85	23.67	24.02
1579	23.68	23.52	23.84
1578	23.87	23.70	24.05

Year CE	SST °C	Lower °C	Upper °C
1577	23.70	23.54	23.86
1576	23.45	23.32	23.58
1575	23.35	23.23	23.47
1574	23.65	23.50	23.80
1573	23.63	23.48	23.78
1572	23.79	23.62	23.96
1571	23.47	23.33	23.60
1570	23.68	23.52	23.83
1569	23.68	23.53	23.84
1568	23.61	23.46	23.76
1567	23.87	23.69	24.05
1566	23.88	23.70	24.06
1565	23.80	23.63	23.97
1564	23.29	23.18	23.41
1563	23.22	23.11	23.33
1562	23.37	23.25	23.50
1561	23.44	23.31	23.57
1560	23.14	23.04	23.25
1559	23.10	23.00	23.21
1558	23.08	22.98	23.18
1557	23.05	22.95	23.15

Year CE	SST °C	Lower °C	Upper °C
1556	23.13	23.03	23.24
1555	23.19	23.08	23.29
1554	23.12	23.02	23.22
1553	23.09	22.99	23.19
1552	23.13	23.02	23.23
1551	23.65	23.50	23.81
1550	23.63	23.48	23.79
1549	23.85	23.67	24.02
1548	23.79	23.62	23.95
1547	23.88	23.70	24.05
1546	23.86	23.69	24.04
1545	23.80	23.63	23.98
1544	24.02	23.82	24.21
1543	23.91	23.73	24.09
1542	23.95	23.76	24.14
1541	23.78	23.61	23.95
1540	23.61	23.46	23.76
1539	23.88	23.70	24.06
1538	23.82	23.65	23.99
1537	23.36	23.24	23.49
1536	23.34	23.22	23.46

Year CE	SST °C	Lower °C	Upper °C
1535	23.78	23.61	23.94
1534	23.77	23.60	23.93
1533	24.11	23.91	24.32
1532	24.01	23.82	24.21
1531	23.66	23.51	23.82
1530	23.86	23.68	24.04
1529	23.88	23.70	24.05
1528	23.10	23.00	23.20
1527	23.14	23.03	23.24
1526	23.31	23.19	23.43
1525	23.62	23.47	23.77
1524	23.86	23.68	24.03
1523	23.91	23.73	24.10
1522	23.82	23.65	23.99
1521	23.56	23.42	23.71
1520	23.39	23.26	23.52
1519	23.20	23.09	23.31
1518	23.18	23.08	23.29
1517	23.91	23.73	24.10
1516	23.79	23.62	23.96
1515	23.61	23.46	23.76

Year CE	SST °C	Lower °C	Upper °C
1514	23.85	23.67	24.02
1513	23.32	23.20	23.44
1512	23.35	23.23	23.48
1511	23.30	23.18	23.41
1510	23.78	23.61	23.94
1509	23.70	23.54	23.86
1508	23.91	23.73	24.09
1507	23.88	23.70	24.06
1506	23.92	23.74	24.10
1505	23.76	23.59	23.92
1504	23.88	23.71	24.06
1503	24.05	23.85	24.24
1502	24.13	23.92	24.34
1501	24.01	23.82	24.20
1500	23.94	23.76	24.13
1499	24.15	23.94	24.36
1498	23.88	23.70	24.06
1497	23.65	23.50	23.80
1496	23.63	23.48	23.79
1495	23.59	23.45	23.74
1494	23.75	23.58	23.91

Year CE	SST °C	Lower °C	Upper °C
1493	24.23	24.01	24.45
1492	24.25	24.03	24.47
1491	23.77	23.60	23.93
1490	23.63	23.48	23.78
1489	23.87	23.69	24.05
1488	23.86	23.69	24.04
1487	23.78	23.61	23.95
1486	23.65	23.49	23.80
1485	24.00	23.81	24.20
1484	23.61	23.46	23.76
1483	23.79	23.62	23.96
1482	23.90	23.72	24.09
1481	23.67	23.51	23.82
1480	23.49	23.36	23.63
1479	23.63	23.47	23.78
1478	23.66	23.50	23.81
1477	23.70	23.55	23.86
1476	23.83	23.66	24.01
1475	23.72	23.56	23.88
1474	23.55	23.41	23.70
1473	23.35	23.23	23.48

Year CE	SST °C	Lower °C	Upper °C
1472	23.77	23.60	23.93
1471	23.80	23.63	23.97
1470	23.90	23.72	24.08
1469	23.91	23.73	24.09
1468	23.53	23.39	23.68
1467	23.64	23.49	23.79
1466	23.68	23.52	23.84
1465	23.34	23.21	23.46
1464	23.47	23.34	23.61

Year CE	SST °C	Lower °C	Upper °C
1463	23.66	23.51	23.82
1462	23.91	23.73	24.09
1461	23.78	23.61	23.95
1460	23.66	23.50	23.81
1459	23.71	23.55	23.87
1458	23.85	23.68	24.03
1457	23.90	23.72	24.08
1456	23.59	23.44	23.73